Polyhedral Oligomeric Silsesquioxane-Based Macroanions to Level Up the Li + Transport Number of Electrolytes for Lithium Batteries

Thi Khanh Ly Nguyen, Trang Phan, Fabrice Cousin, Didier Devaux, Sumit Mehan, Fabio Ziarelli, Stéphane Viel, Didier Gigmes, Priscillia Soudant, Renaud Bouchet

To cite this version:

Thi Khanh Ly Nguyen, Trang Phan, Fabrice Cousin, Didier Devaux, Sumit Mehan, et al.. Polyhedral Oligomeric Silsesquioxane-Based Macroanions to Level Up the Li + Transport Number of Electrolytes for Lithium Batteries. Chemistry of Materials, 2022, 34 (15), pp.6944-6957. 10.1021/acs.chemmater.2c01325 . hal-03765974

HAL Id: hal-03765974
https://hal.science/hal-03765974v1

Submitted on 31 Aug 2022

HAL is a multi-disciplinary open access archive for the deposit and dissemination of scientific research documents, whether they are published or not. The documents may come from teaching and research institutions in France or abroad, or from public or private research centers.

L'archive ouverte pluridisciplinaire **HAL**, est destinée au dépôt et à la diffusion de documents scientifiques de niveau recherche, publiés ou non, émanant des établissements d'enseignement et de recherche français ou étrangers, des laboratoires publics ou privés.

(Polyhedral Oligomeric Silsesquioxane)-based macro-anions to level up the Li^+ transport number of electrolytes for lithium battery

Thi Khanh Ly NGUYEN[1,†], *Trang N. T. PHAN*[2,*], *Fabrice COUSIN*[3], *Didier DEVAUX*[1], *Sumit MEHAN*[3], *Fabio ZIARELLI*[4], *Stéphane VIEL*[2], *Didier GIGMES*[2], *Priscillia SOUDANT*[1], *Renaud BOUCHET*[1,*]

[1]Univ. Grenoble Alpes, Univ. Savoie Mont Blanc, CNRS, Grenoble INP, LEPMI, 38000 Grenoble, France

[2]Aix Marseille Univ, CNRS, ICR, 13397 Marseille, France

[3]Laboratoire Léon Brillouin, Université Paris-Saclay, CEA-CNRS UMR 12, 91191 Gif-sur-Yvette, France

[4]Aix Marseille Univ, CNRS, Fédération des Sciences Chimiques de Marseille (FR 1739), 13397 Marseille, France

ABSTRACT Increasing lithium transport number in liquid and polymers electrolytes is an important task for higher power performance since it limits the promotion of concentration gradient and the mitigation of dendrite nucleation. One promising route to limit the anion mobility is the design of macro-anions. In this paper, by varying the number of LiTFSI salt and

PEG chains attached to POSS nanoparticles, a series of POSS-based macro-anions were synthesized and complexed with tetraglyme (TEG) model solvent to form electrolytes at different concentrations from EO/Li=10 to 25. While a high transport number in between 0.7 to 0.86 was obtained as expected, a significantly lower cationic conductivity was observed compared to TEG-LiTFSI reference electrolyte at the same lithium concentration. The understanding of this behavior is necessary for the design of the next electrolyte generation. Thus, a complete study coupling morphologic (SAXS), thermal (DSC/ATG), conductivity (EIS), and ^{1}H, ^{7}Li, ^{19}F diffusion NMR analyses is provided to establish in a single equation (Equation 11) the relationship between the Li^{+} ionic transport properties and the size of macro-anion which impacts strongly, beside the transport number, the electrolyte bulk properties, such as the viscosity and the tortuosity induced by the large POSS inorganic cores. In addition, it is shown that the chemical affinity of the organic POSS shell and the solvent pilots the Li^{+} dissociation rate, and thus the content of free Li^{+} ion. These results provide a deep insight on the intricacy of the physical properties (Equation 11) that leads to high cationic conductivity which can be a helpful intellectual platform for the target-design of new macro-anions.

INTRODUCTION

Lithium metal (Li) with its high specific capacity, ten times higher than graphite, and low redox potential is seen as the next reference material for negative battery electrode.[1] However, the nucleation and growth of Li dendrites through the electrolyte during the recharge, leading to battery failure, still remain the major drawback that limits its widespread use.[2] Theoretically, the nucleation of Li dendrites can be prevented by increasing Li cation transference number[3] while stiff electrolyte can mitigate their growth.[4] The latter is clearly in favor of solid-state electrolytes (polymer and ceramic). In case of polymer electrolytes, the stiffness seems indeed to play a positive role[5] to increase the time before short-cuts due to lithium dendrites.[6] However, when the polymer is too stiff, the Li/Polymer interface suffers from poor interfacial wetting requiring additional external pressure. In addition, the polymer-based battery can only operate today at temperature higher than 60°C to reach sufficient conductivity ($>10^{-4}$ S cm^{-1}). In case of ceramic electrolytes while they present high conductivity at room temperature, several studies have described dendrites growth,[7–9] especially through the grain boundaries, showing that other parameters than the electrolyte stiffness are at stake, for instance the materials reactivity with the Li surface. Another approach is to increase the Li^+ transference number. While that of ceramic electrolytes is typically of unity, polymer electrolytes requires specific functionalization such as anion-grafting onto the backbone to immobilize them.[10–12] However, the main lock for this family of materials is the low ionic conductivity at room temperature ($<10^{-6}$ S cm^{-1}). Besides, non-flammable liquid electrolytes have advantage over solid ones as they can easily penetrate inside the porosity of the composite electrodes so that most of the active materials are accessible and the corresponding impregnation process is already implemented at an industrial scale. Therefore, increasing the Li^+ transference number of non-flammable liquid electrolytes could be an avenue to develop safe and reliable Li metal battery[13,14] operating at room temperature.

In liquid electrolyte, the ionic mobility is inversely proportional to the size of the solvated ion thanks to the viscous hindrance of the liquid electrolyte (Stokes-Einstein relationship), thus a simple strategy is to replace conventional compact anions such as PF_6^-, by bulky anions, referred as macro-anion.[15–17] For example, by attaching longer chain to BF_4^- anion, a slight increase in t_{Li}^+ to 0.48 was reported in propylene carbonate solvent.[16] Multi charge anions were also developed to get an additional diminution of salts pairing and aggregation[18–20] with a t_{Li}^+ of 0.73 for trilithium 2,2′,2″-tris(trifluoromethyl)benzotris(imidazolate) (Li_3BTI) salt in carbonates solvents.[20] Anionic polymer dissolved in a non-aqueous solvent such as dimethyl sulfoxide and used as liquid electrolytes is also a good compromise to attain both high room temperature conductivity (10^{-3} S cm^{-1}) and t_{Li}^{+} (0.8).[21]

Macro-anions based on the grafting of anions onto an inorganic nanoparticles such as SiO_2 [22–24] has recently gained some interests due to their attractive synergy between conductivity and improvement of mechanical properties. An adequate room temperature conductivity of 10^{-4} S cm^{-1} with a t_{Li}^{+} between 0.6 and 0.9 can be achieved for an electrolyte comprising SiO_2 grafted with SO_3BF_3Li salt complexed in tetraethylene glycol dimethyl ether (TEG).[23] Recently, polyoctahedral silsesquioxane (POSS) were reported as battery electrolytes additives thanks to their small size, flame retardancy, good thermal stability, and capabilities to multi-functionalized their end-functions.[25] Many authors have demonstrated the enhancement in thermal and electrochemical stability, and ion conductivity of polymer electrolytes made of a dispersion of poly(ethylene glycol) (PEG) grafted POSS in PEO matrice,[26–28] a direct grafting of POSS molecules onto PEO backbones,[29–31] and cross-linked polymer/siloxane networks.[32,33] Other routes were investigated including the use of POSS-PEG laden with LiTFSI acting directly as an electrolyte,[34,35] the grafting of anion to produce new Li bulky salts,[36–38] and the mixing of the latter two (POSS-PEG and Lithium bulky salt) to produce single-ion conducting electrolyte.[36] Wunder's group has reported some remarkable results by using functionalized POSS in Li batteries. By mixing a liquid electrolyte (POSS-$(PEG)_8$) and a Li salt (POSS-$(BF_3Li)_3$), they measured a room temperature conductivity of 2.50×10^{-4} S cm^{-1} with a t_{Li}^{+} of 0.5.[36] Recently, the same authors reported on a functionalized POSS with 8 functions of $LiNSO_2CF_3$ group through the alkylsilanes reaction and used it as Li salt in TEG electrolytes reaching at 25°C conductivity of 2×10^{-4} S cm^{-1} with a t_{Li}^{+} of 0.65.[39,40] The authors also compared the transference number of Li^{+} measured thanks to diffusion NMR or an electrochemical method and related the difference between the two methods to the low dissociation of Li^{+} in the electrolytes. However, this value was not quantified. Batteries made of a lithium negative electrode and a $LiFePO_4$ positive electrode were tested using a salt mixture between LiTFSI and POSS-$(TFSI)_8$ in TEG. They showed a stable cycling with high capacity retention between C/2 and 2C.

Herein, following the concept of both macro-anion and POSS-based Li salt, we propose a deep analysis of the structural (SAXS), thermal (DSC/ATG), and ionic transport properties (PFG-NMR, EIS) of functional POSS, as macro-anionic Li salt, dispersed in TEG as liquid electrolytes. TEG has been chosen as a reference solvent thanks to its ability to strongly coordinate Li^{+} and form a quite stable interface versus lithium[14]. Three types of functionalized POSS were synthesized with either only TFSI-grafted based anions, or both TFSI and PEG grafted with two different PEG/TFSI ratios. Different liquid electrolytes were then prepared and studied as a function of the POSS concentration and related functional nature. The influence of these parameters on the ionic transport properties throughout the intricacy of the viscosity, Li^{+} transport number, dissociation rate of the POSS based Li salt, and the tortuosity induces by the large size of the POSS anion, has been uncovered thanks to a macroscopic model that can be used as the manual to optimize the macro-anions design.

EXPERIMENTAL

Materials.

Poly(ethylene glycol) methyl ether (MPEG) with with an average molecular weight, M_n, of 550 g mol^{-1}, epibromohydrin (99 %), sodium hydride (60 % dispersion in mineral oil), tetraethylene glycol dimethyl ether (tetraglyme or TEG, >99%), lithium bis(trifluoromethane)sulfonimide (LiTFSI, >99,95%) were purchased from Aldrich. The octakis(3-ammoniumpropyl)octasilsesquioxane octachloride (POSS-$NH_2.HCl$) was synthesized according to the published procedure[41]. The potassium vinyl sulfonyl(trifluoromethane sulfonyl)imide (vinyl-KTFSI) was prepared as described in our previous work.[42] All solvents and other reagents were synthesis grade and were used without further purification.

Characterization

Nuclear Magnetic Resonance (NMR). ^1H, ^{19}F and ^7Li NMR spectra were recorded on a Bruker AVANCE 400 MHz machine using deuterated DMSO-d_6 as the solvent.

Pulsed Field Gradient Nuclear Magnetic Resonance (PFG-NMR) experiments were carried out at 60°C on a Bruker AVANCE III-HD 400 MHz (^1H Larmor frequency) NMR spectrometer to measure the lithium (^7Li) and fluorine (^{19}F) self-diffusion coefficients of the electrolytes. These experiments were conducted using a commercial High-Resolution Magic-Angle Spinning (HRMAS) triple-resonance 4 mm probe head from DOTY Scientific, which was equipped with a ^2H lock channel and a magnetic field gradient coil aligned along the magic-angle spinning axis. The samples were analyzed as such without solvent in a 4 mm DOTY MAS NMR rotor with ULTEM inserts to achieve an active volume of 20 µL (the sample weight was not measured). No sample spinning was applied. The samples were previously prepared and stored under Ar atmosphere. The NMR spectra were processed with 20 Hz line broadening prior to phase and baseline corrections. For each PFG-NMR experiment, 16 quadratically spaced gradient values with an approximately square shape were used between 6% and 95% of the maximum gradient strength (which was calibrated to be 250 $G.cm^{-1}$), and the self-diffusion coefficients were estimated by fitting the obtained signal decays on the Bruker Topspin software using the Stejskal-Tanner equation:[43]

$$\ln(\frac{S}{S_o}) = -D\gamma^2 G^2 \delta^2 (\Delta - \frac{\delta}{3}) \text{ (Equation 1)}$$

where γ is the gyromagnetic ratio of the nucleus under study, Δ the diffusion time, δ the gradient pulse duration, D the self-diffusion coefficient, and S and S_0 are the intensities of the obtained signals with and without gradient pulses, respectively.

Small Angle X-ray Scattering (SAXS). Measurements were carried out on a Xeuss 2.0 HR instrument from Xenocs at room temperature. The instrument uses a microfocused Cu Kα source with a wavelength of 1.54 Å and a PILATUS3 detector (Dectris, Switzerland). The experiments were performed at two different sample-to-detector distances, respectively 2480 mm with a collimated beam size of 0.5 × 0.5 mm and 540 mm with a collimated beam size of 0.8 × 0.8 mm to achieve a broad q-range of 0.0045 $Å^{-1}$ – 1.2 $Å^{-1}$. Inside an Ar filled glove box, the solutions were injected into glass capillaries then sealed. Experiments were performed respectively at room temperature and at 60°C. Samples were placed onto a home-made sample holder thermalized with a circulating water flow coupled with a Huber bath, allowing to control the samples temperature up to 65°C. Scattering from the empty beam, empty capillary and dark field were measured independently and subtracted from the sample scattering to obtain scattering in absolute units. At very large q ($q > 0.4$ $Å^{-1}$), the samples scattering was completely dominated by the contribution from TEG solvent which was then properly subtracted from the samples. Therefore, only the data within the 0.0045 $Å^{-1}$ – 0.45 $Å^{-1}$ range are shown in this study.

Differential Scanning Calorimetry (DSC) was performed on a 1 STARe System from Mettler-Toledo under nitrogen flow (50 $mL.min^{-1}$) and a heating rate of 20 °C min^{-1} and cooling rate of 5 °C min^{-1}. The samples are prepared in the glove box using tighten aluminum crucible.

After one heating up to 100°C and cooling down to 100°C, the glass transition temperature (T_g) and the melting temperature of the sample were evaluated through the second heating up to 100°C.

The crystallinity degree (χ) of TEG in these electrolytes can be calculated thanks to the measured melting enthalpy divided by the mass of TEG in the sample (ΔH_m (J per gram of TEG)):

$$\chi_{relative} = \frac{\Delta H_{mTEG}}{\Delta H_o} \times 100\% \text{ (Equation 2)}$$

with ΔH_o the melting enthalpy of a pure TEG taken at 133 J g^{-1} from literature.[44]

Thermogravimetric Analysis *(TGA)* was conducted on a 1 STARe System analyzer from Mettler-Toledo using alumina crucibles varying the temperature from 25 to 600 °C at a heating rate of 10 $°C.min^{-1}$ with an isotherm of one hour at 100 °C. A constant nitrogen flow of 50 mL min^{-1} is set.

Ionic Conductivity was determined using micro platinized-platinum conductivity cells (Hach-Lange) from electrochemical impedance spectroscopy carried out thanks to a Hewlett Packard 4192A with an excitation voltage of 40 mV in the frequency range spanning 13 MHz to 5 Hz. The cells were placed inside a Vöetsch VC4018 climatic chamber where the temperature (T) was varied from 25 up to 55 then down to -15 °C. The impedance spectra (see Figure S1) were recorded by steps of 5 ± 0.1 °C after a stabilization time of 1 h minimum. The ionic conductivity (σ) was calculated from the resistance of the electrolyte[45] extracted at high frequency by:

$$\sigma(T) = \frac{k}{R_{electrolyte}} \text{ (Equation 3)}$$

where k is the cell constant calibrated at 25°C using KCl solutions at 0.1M and 1M.

***Cationic transference number* (t_{Li}^{+})** was determined by different methods. Firstly, thanks to PFG-NMR results, t_{NMR}^{+} is calculated using the diffusion coefficients of lithium cation (D_{Li}) and fluorine based macro-anion (D_{F}) and their respective charge (z_{+}=1, z_{-}) according to:

$$t_{NMR}^{+} = \frac{C_{+}z_{+}^{2}D_{Li}}{C_{+}z_{+}^{2}D_{Li} + C_{-}z_{-}^{2}D_{F}} = \frac{D_{Li}}{D_{Li} + z_{-}D_{F}} \text{ (Equation 4)}$$

Secondly, $t_{El.}^{+}$can be estimated using electrochemical methods, by coupling techniques of DC polarization (10 mV or 30 mV), *i.e.*, chronoamperometry technique, and AC impedance spectroscopy using a Li /Li symmetric cell in coin-cell configuration comprising a glass-fiber separator (Freudenberg) impregnated with the studied electrolyte. Impedance measurements were carried out before and after applying the DC polarization (ΔV). Transference number was then calculated using the equation proposed in Watanabe *et al.*:[46]

$$t_{El.}^{+} = \frac{R_{electrolyte}}{(\frac{\Delta V}{I_{s}} - R_{s})} \text{(Equation 5)}$$

with R_{s} the interface resistance after polarization, and I_{s} the steady-state current reached at the end of polarization (*ca* three hours) (Figure S2).

Materials synthesis

The synthesis of POSS-TFSI and POSS-TFSI-PEG anions was performed according to Scheme S1. First, the octakis(3-ammoniumpropyl)octasilsesquioxane octachloride (POSS-*NH$_2$.HCl*) was neutralized to octakis(3-aminopropyl)octasilsesquioxane (POSS-*NH$_2$)* and then POSS-*NH$_2$* was reacted either with lithium vinyl sulfonyl(trifluoromethane sulfonyl)imide (vinyl-LiTFSI) or both with vinyl-LiTFSI and epoxide-terminated methoxy-poly(ethylene glycol).

Synthesis of epoxide-terminated MPEG (epoxy-MPEG). Epoxy-MPEG was prepared according to a literature procedure with some adaptations.[47] Briefly, MPEG of 550 g mol^{-1} (10.0

g, 18.2 mmol) was dissolved in 60 mL of toluene and dried by azeotropic distillation using a Dean-Stark apparatus. The hydroxy-end group of the MPEG was then converted into sodium alkoxide by its reaction with sodium hydride (1.09 g, 27.3 mmol) at 40 °C for 2 hours. After this time, epibromohydrin (3.2 mL, 36.4 mmol) was slowly added to the solution and the mixture was stirred at 40°C overnight. After the reaction, the mixture was filtered and the polymer was precipitated in diethyl ether, filtered, washed with diethyl ether and dried under vacuum at room temperature. The coupling yield was quantitative.

Synthesis of lithium vinyl sulfonyl(trifluoromethane sulfonyl)imide (vinyl-LiTFSI). Amberlite IR-120-H form ion-exchange resin (30g) was successively washed with deionized water (2 x 100 mL), 1M LiOH (3 x 100 mL), and deionized water (6 x 100 mL) until obtaining a neutral pH. The resin beads were then loaded into a column of 3.5 cm outside diameter. Elution across the column of 4.5 g of vinyl-KTFSI dissolved in 20 mL of water, produced an aqueous solution of vinyl-LiTFSI. Water was removed by a rotary evaporator at 50 °C. The lithium salt was dried under vacuum at 60 °C for 24 h and stored under argon.

Synthesis of POSS functionalized with lithium salt (POSS-TFSI). Amberlite IRA-400 ion-exchange resin (30 g) was prepared by successive washing with water (4 x 150 mL), 1M NaOH (3x150 mL), water (6x150 mL), and methanol (6x150 mL), which was the elution solvent; the resin was suspended in eluent and chilled (-10 °C, 2 h) before use. Half of the resin beads were loaded into a column (3.5 cm outside diameter), and the other half were used to dissolve a suspension of POSS-NH_2.HCl (1.35 g, 1.15 mmol) in the minimum amount of methanol below 0°C. Elution across the column produced a methanol solution of neutralized POSS-NH_2. Immediately, vinyl-LiTFSI, previously prepared (3.62g, 14.33 mmol), dissolved in 10 mL of methanol were added to the solution of neutralized POSS-NH_2. The resulting mixture (50 mL) was loaded in a round bottom flask equipped with a condenser and placed in an oil bath preheated at 80°C. The mixture was kept under magnetic stirring at this temperature for two days. At the end of this period, the produced Li salt grafted POSS, denoted as POSS-TFSI, was separated from the free Li salt using a Millipore Ultra-filtration apparatus equipped with an Ultracel® membrane filter of 3 kDa pore diameter. The solution was filtered three times, each time, 50 mL of the obtained solution was diluted with 200 mL of methanol and concentrated to the initial volume. Functionalized POSS solution in methanol was stored in a fridge until use. The chemical structure of the POSS-TFSI is presented in Scheme 1 while the experimental data of this synthesis are summarized in Table 1.

Scheme 1. Chemical structure of synthesized macro-anion POSS-TFSI and POSS-TFSI-PEG

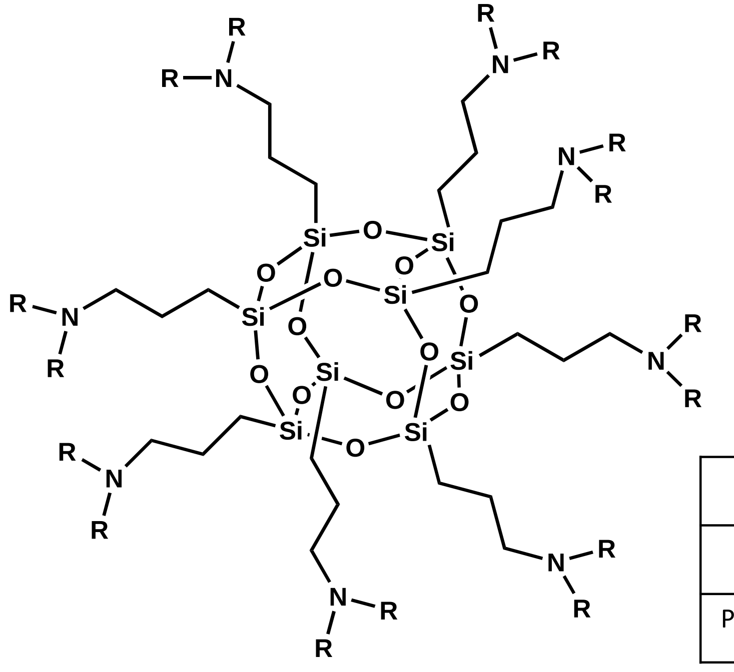

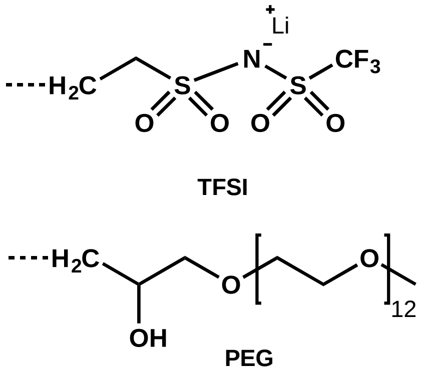

POSS type	R
POSS-TFSI	TSFI and/or H
POSS-TFSI-PEG	TFSI and/or H and/or PEG

Synthesis of POSS functionalized with lithium salt and poly(ethylene glycol) (POSS-TFSI-PEG). A similar methodology to synthesize POSS-TFSI was used to produce TFSI/PEG-grafted POSS. As for the POSS-TFSI, after the filtering step, the functionalized POSS were diluted in methanol and stored in a fridge until use. These materials are denoted POSS-TFSI-PEG$_x$ with x

the molar ratio of PEG over Lithium within the POSS molecules. Two compounds have been prepared and the experimental data of these synthesis are given in Table 1.

Table 1. Synthesis details for the preparation of functionalized POSS compounds (POSS-TFSI and POSS-TFSI-PEG$_x$) and the characteristics of resulting products.

Entry	Functionalized POSS	$m_{POSS-NH2}$ *g, (mmol)*	$m_{viny-LiTFSI}$ g, (mmol)	$m_{epoxy-PEG}$ g, (mmol)	N_{LiTFSI}/POSS^a	N_{PEG}/POSS^a	$M_{modified-POSS}$^{b} g.mol^{-1}	PEG/Li ratio	T_g (°C)	Measured density (g cm^{-3})
1	POSS-TFSI	1.35 (*1.05*)	3.62 (*14.33*)	0	10	0	3321	0	--	1.99±0.02
2	POSS-TFSI-PEG$_{0.7}$	1.20 (*0.92*)	1.91 (*7.42*)	4.58 (*7.41*)	8	5.6	6243	0.7	-37	1.43±0.01
3	POSS-TFSI-PEG$_{0.4}$	1.20 (*0.92*)	1.68 (*6.51*)	2.43 (*3.93*)	6.6	2.7	4194	0.4	-24	1.55±0.02

[a] Experimental number of Li salt molecules or PEG chains par POSS molecule, values determined by ^{1}H NMR analysis. [b] Calculated molar mass of the modified POSS molecules based on NMR data.

Preparation of liquid electrolytes

To formulate the liquid electrolytes, the POSS-TFSI and POSS-TFSI-PEG$_x$ were first recuperated from methanol solutions by rotary evaporation. Then, they were dried under vacuum at 60 °C for 24 hours before being mixed with the desired amounts of TEG in an argon (Ar) filled glove box (O_2 and H_2O < 1ppm, Campus, Jacomex) and stirred overnight at room temperature. The electrolytes are denoted POSS-TFSI-*y* with *y* the molar EO/Li ratio and POSS-TFSI-PEG$_x$-*20*, respectively**.** A reference electrolyte made of TEG laden with LiTFSI in a molar ratio EO/Li of 20, and denoted LiTFSI-20, was also formulated. The experimental data for the preparation of liquid electrolytes are summarized in Table S1. The compositions of all the prepared liquid electrolytes are given in Table 2. The density, the lithium concentration and the volume fraction of the POSS in the different electrolytes are also given. The latter was calculated using the volume value of each compound reported in Table S1.

RESULTS AND DISCUSSION

A- Preparation of liquid electrolytes composing of lithium salt-grafted POSS and TEG

A.1. *Synthesis and structural characterization of lithium salt-grafted POSS*

Prior proceeding to the preparation of LiTFSI-grafted POSS and LiTFSI/PEG-grafted POSS, we need to synthesize the appropriated lithium salt and introduce the right functional group to methoxy-PEG. For this purpose, α-methoxy-PEG (MPEG) of 550 g mol^{-1} was end-capped by an epoxy group at the ω-position. The ω-hydroxy end group of MPEG was deprotonated by sodium hydride and then reacted with epichlorohydrin in toluene. The sodium chloride byproduct formed a precipitate in toluene thereby allowing a shift in the reaction equilibrium toward the expected α-methoxy- ω-epoxy-PEG. The ^{1}H NMR spectrum of epoxide-terminated MPEG is shown in Figure S3. The spectrum exhibits key signals corresponding to the expected structure of epoxy-MPEG. The signals at 3.63 and 3.37 ppm correspond to the methylene protons of the ethylene oxide units and the methoxy α-end group respectively (labelled *b,a*), whereas those at 3.14, 2.78 and 2.60 ppm were attributed to the protons of the epoxide end group (labelled *c, d, e*). The epoxidation yield was estimated from the relative integral value of the peaks (*a*) and (*c*). This ratio was close to 3:1, indicating a quasi-quantitative conversion of the hydroxy-end group of MPEG into an epoxy unit.

The approach selected to graft lithium salt to amino-POSS molecule was the Michael addition reaction. Vinyl-LiTFSI was demonstrated as the most efficient reactant in this kind of reaction.[42] It was prepared by exchanging potassium ions to lithium ions of vinyl-KTFSI using ion-exchange resin process. The cation exchange was quantitative and confirmed by ^{1}H, ^{7}Li and ^{19}F NMR analysis. These spectra are shown in Figures S4 – 6 and compared to those of vinyl-KTFSI. As we can see, the ^{1}H NMR spectra of potassium vinyl-TFSI and lithium vinyl-TFSI are identical (Figure S4) while ^{19}F NMR spectrum of lithium vinyl-TFSI shows a slightly shift compared to that of potassium vinyl-TFSI (Figure S5). The presence of lithium ions is well indicated in the ^{7}Li NMR spectrum (Figure S6).

The grafting of lithium salt and MPEG to POSS molecule was carried out in methanol in reflux. The grafting yield and the chemical composition of the resulting products was determined by ^{1}H NMR. The ^{1}H NMR spectrum of POSS functionalized with lithium salt (POSS-TFSI) presented in Figure S7 exhibits the presence of signals of the expected Michael adduct at 3.09, ppm labeled, (e) and 2.85 ppm, labeled (d), corresponding to the protons of $–CH_2CH_2SO_2N^{(-)}SO_2CF_3$ (ethyl-TFSI) anion, while those at 0.59 ppm, labelled (a), and 1.44 ppm, labeled (b), are characteristics of CH_2 protons near the POSS core. In addition, the presence of TFSI functionality was also confirmed by ^{19}F and ^{7}Li NMR analysis with the fluorine and lithium signal at -77.56 ppm (Figure S8a) and at -1.03 ppm (Figure S8b), respectively. The number of lithium salts grafted to the POSS core was determined by ^{1}H NMR analysis based on the relative integral value of the peaks (d) and (a). This ratio was 1.245 that corresponds to 9.96 (or 1.245 x 8) lithium salt moieties per POSS molecule. So, the average molar mass of POSS-TFSI can be calculated and equal to 3321 g mol^{-1} ($M_{POSS\text{-}TFSI} = M_{POSS\text{-}NH2} + 9.96 * M_{ethyl\text{-}LiTFSI} – 9.96 * M_H$).

Concerning the POSS functionalized with lithium salt and PEG (POSS-TFSI-PEG), they are also characterized by ^{1}H NMR. The ^{1}H NMR spectra of two POSS-TFSI-PEG$_x$ are shown in Figures S9 and S10, respectively. In addition to the characteristics signals of the protons of ethyl-TFSI, the presence of PEG grafted to POSS core is evidenced by the peaks of CH_3-O- methoxy end group at 3.24 ppm and $-CH_2-CH_2-O-$ methylene protons of PEG at 3.51 ppm. By comparing the relative integral value of the peaks of ethyl-TFSI group (peak *d*) and CH_3-O- methoxy end group of PEG (peak *f*) with that of amino-POSS (peak *a*), we can estimate the number of lithium salt molecules and PEG chains grafted on the POSS core. These values are given in Table 1. Thus, the average molar mass of the two POSS-TFSI-PEG compounds can be estimated based on these ratios ($M_{POSS\text{-}TFSI\text{-}PEG} = M_{POSS\text{-}NH2} + N_{LiTFSI/POSS} * M_{ethyl\text{-}LiTFSI} - N_{LiTFSI/POSS} * M_H + N_{PEG/POSS} * M_{epoxy\text{-}MPEG}$) and equal to 6243 g mol^{-1} and 4194 g mol^{-1} for POSS-TFSI-PEG$_{0.7}$ and POSS-TFSI-PEG$_{0.4}$ respectively. The composition of functionalized POSS and their molar mass are given in Table 1.

A.2. Density measurement of liquid electrolytes

Density of all electrolytes was determined at 25°C by pycnometry using a 1ml pycnometer. All measures were realized in a dry glove-box (Jacomex, O_2, H_2O# 1ppm) to ensure the dryness of the atmosphere. Precise volume of the pycnometer was recalibrated using dry hexane and three successive measures of electrolyte weight using a Mettler Toledo FS GRAM balance were conducted. In case of solid POSS-TFSI, the weight difference of pycnometer containing only hexane or hexane and POSS allowed the calculation of POSS-TFSI density. The measured density of the electrolyte (d_{el}) and the theoretical Li$^+$ concentration ($C_{Li}{}^+$), calculated using Equation 6, are added in Table 2. In Figure S11, the density of the POSS-TFSI-*y* electrolytes is plotted as a function of the mass fraction of Li salt either based on POSS or LiTFSI salts. In addition, the evolution of the density assuming an ideal mixture (*i.e.* the total volume being the sum of the volume of the neat components (TEG and salts)) for all electrolytes is plotted as reference in Figure S11.

$$C_{Li}^{+} = \frac{n_{Li}}{V_{electrolyte}} = C_{modified\ POSS} \times x_{Li/salt} = \frac{x_{Li/salt} \times d_{el} \times \%wt_{salt}}{M_{salt}} \quad \text{(Equation 6)}$$

where $\%wt_{salt}$ is the mass fraction of salt in electrolytes, d_{el} is the measured density of the electrolytes listed on Table 2, M_{salt} and M_{TEG} are the molecular weight of salt (Li-grafted-POSS or LiTFSI) and tetraglyme, respectively, and $x_{Li/salt}$ is the number of Lithium per salt molecule (assuming a full salt dissociation).

One can note that the concentrations obtained taking the measured densities are roughly similar to typically values obtained from ideal mixture with only 10 to 30 % difference (Figure S11).

Table 2. Composition of the POSS-TFSI and POSS-TFSI-PEG electrolytes.

Sample	ion charge		Salt concentration (wt%)		TEG concentration (wt%)		PEG concentration (wt%)		$d_{measured}$[b] (g cm^{-3})	C_{Li^+} (mol L^{-1})	Vol% of modified POSS ε_{POSS} (%)
	z_+	z_-	NMR	TGA[a]	NMR	TGA[a]	NMR	TGA[a]			
LiTFSI-20	1	1	21	23	79	77	--	--	1.21 ± 0.02	0.86	--
POSS-TFSI-10	1	10	38	43	62	57	--	--	1.34 ± 0.05	1.50	24.9
POSS-TFSI-15	1	10	29	30	71	70	--	--	1.31 ± 0.01	1.12	18.1
POSS-TFSI-20	1	10	23	23	77	77	--	--	1.28 ± 0.02	0.88	14.1
POSS-TFSI-25	1	10	19	20	81	80	--	--	1.24 ± 0.03	0.72	11.7
POSS-TFSI-PEG$_{0.7}$-20	1	8	57	59	43	41	31	32	1.32 ± 0.03	0.96	50.5
POSS-TFSI-PEG$_{0.4}$-20	1	6.6	44	54	56	46	18	24	1.37 ± 0.02	0.96	36.1

[a] Values recalculated from TGA curves assuming that the second degradation process is 100% due to LiTFSI chain.

[b] Error values obtained from three successive measures.

B- Dispersion and interaction of POSS-salts with tetraglyme

To get insight on the dispersion state of the electrolyte, SAXS was performed on all the electrolytes listed in Table 2. All samples were measured three times, twice at room temperature with an elapsed time of around 1 year between the two series of experiments, and then at 60°C. Remarkably, the SAXS pattern of all samples at room temperature does not evolve over 1 year, demonstrating the perfect structural temporal stability of the samples (Figure S12). At 60° C, the structure does not change for the POSS-TFSI-PEG$_x$-*20* samples, an only slightly evolves for the

POSS-TFSI-*y* samples. For these last samples, the aggregation depicted hereafter slightly increases upon temperature increase without changing internal aggregate morphology (see supplementary material).

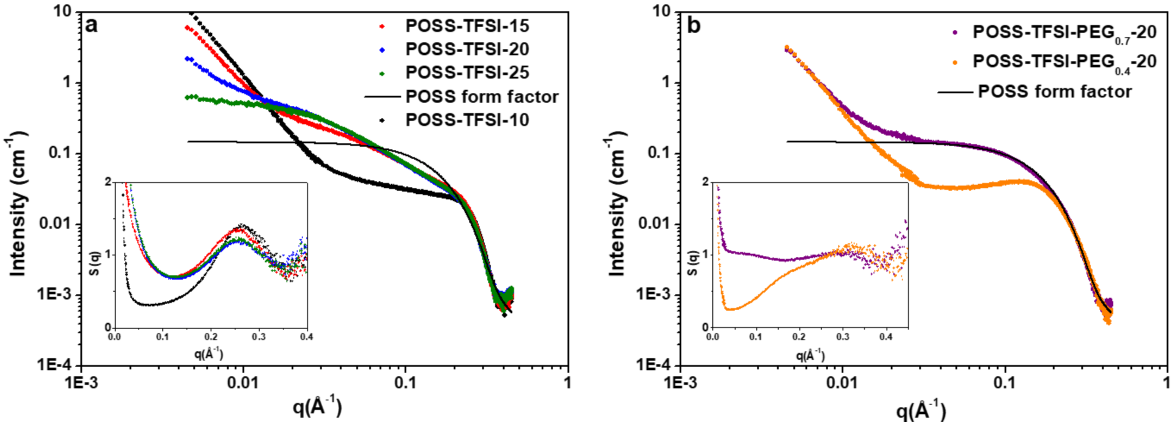

Figure 1. SAXS measurements at room temperature. (a) POSS-TFSI-*y* samples. Inset: structure factors. (b) POSS-TFSI-PEG$_x$-*20* samples. The continuous line corresponds to the form factor $P_{POSS}(q)$ fitted with a form factor of a sphere. All curves have been scaled to a factor in the 0.8-1.1 range to overlap at large q with $P_{POSS}(q)$.

Figure 1 shows the scattering intensity I(q) *versus* q for the different samples in log-log representation. Assuming that the POSS molecules are centro-symmetric objects, the scattering density I(q) can be expressed by the general following equation:

$$I(q) = \ \phi\, \Delta\rho^2\, P_{POSS}(q)\, S(q) \qquad \text{(Equation 7)}$$

where ϕ is the volume fraction of POSS grafted molecules; $\Delta\rho$ is the difference of electron scattering length density between the POSS grafted object and TEG; $P_{POSS}(q)$ is the form factor of the grafted POSS molecules; $S(q)$ is the structure factor.

For all samples, I(q) shows the typical behavior of the Porod law (~ q^{-4}) at the largest q which is characteristic from the scattering of 3D objects. This is mainly ascribed to the form factor of the POSS grafted molecules, $P_{POSS}(q)$, due to contrast reasons. Indeed, the contrast comes from the square of the difference of electron scattering length density between the object, herein the grafted POSS molecule that contains Si and S atoms with significantly larger electrons number than atoms of the surrounding media, *i.e.* the TEG. In the case of the POSS-TFSI-PEG$_x$-*20*, the outer grafted PEG chains are completely invisible since they have almost exactly the same ρ_e as the solvent molecules (TEG).

At large q, the scattering of all samples except for POSS-TFSI-PEG$_{0.4}$-20 shows a strong correlation peak at ca 0.25 Å^{-1} for POSS-TFSI-y and at 0.16 Å^{-1} for POSS-TFSI-PEG$_{0.7}$-20 (see insets structure factors in figure 1). In addition, the scattering of POSS-TFSI-PEG$_{0.4}$-20 sample with no correlation peak at large q recalls the one of the pure form factors of spheres (Figure 1). $P_{POSS}(q)$ form factor was then determined by fitting the scattered intensity of the POSS-TFSI-PEG$_{0.4}$-20 by the form factor of spheres with lognormal polydispersity (Đ) on radii for $q > 0.03$ Å^{-1} (Figure 1b), with $R_0 = 10.8$ Å and Đ = 0.2, *i.e.* a mean radius R_{mean} of 11.5 Å.

Given that POSS molecules are centro-symmetrical objects, $P_{POSS}(q)$ also permits to obtain the structure factor $S(q)$ of the POSS molecules that probes the correlations between their centers of mass as $S(q) \propto I(q)/ P_{POSS}(q)$. $S(q)$ is displayed in the inset of Figure 1 a for the POSS-TFSI-y samples and allows to have a better insight of the intensity and position of the correlation peak. It is located at $q^* = 0.272$ Å^{-1} for the POSS-TFSI-10 sample, which gives a distance in direct space of 23.1 Å ($= 2\pi/q^*$) that corresponds to the expected value for two objects in contact (2 x R_{mean}) revealing the existence of POSS aggregates. For the other samples, q^* is very slightly shifted towards lower q values (0.26 Å^{-1}, 24.2 Å in direct space) revealing that they are made of slightly less compact aggregates. The low q part of $S(q)$ enables to determine the morphology of the aggregates. For the POSS-TFSI-25 sample, it shows a q^{-1} decay at intermediate q and tends towards a Guinier plateau at low q. It is thus made of small aggregates that have an overall linear shape, the power law being directly related to their fractal dimension D_f ($I(q) \propto q^{-Df}$), and are perfectly dispersed, with a mean aggregation number N_{agg} of ~ 4, as obtained from $S(q)_{q \rightarrow 0}$. It is markedly different for the POSS-TFSI-10 sample which shows a typical decay in ~ q^{-3}, suggesting the presence of large density fluctuations in the system that arise from the arrangements of aggregates. The structures of the other POSS-TFSI-y samples are intermediate between these two extreme cases, as they present the characteristic features of both the shape of the small linear aggregates at intermediate q and rise at low q due to large heterogeneities.

Concerning POSS-TFSI-$PEG_{0.4}$-20 sample, the rise of low *q* describes the coexistence of large aggregates inside electrolytes at the same time with well-dispersed nanoparticles. The scattering of POSS-TFSI-$PEG_{0.7}$-20 on the other hand shows a correlation peak located at ~ 0.16 Å^{-1} (~ 40 Å in direct space) corresponding to the contact between objects of 20 Å versus 11.5 Å due to PEG grafted shell (in average 8,5 Å thick, in very good agreement with the gauss radius of the grafted PEG).

Overall, despite different behaviors observed for the scattering depending on the POSS type and POSS concentration, all samples appear to contain aggregates. This phenomenon can be explained by high volume ratio of inorganic POSS nanofillers in the electrolytes, as explained by Wunder *et al.* as solvent-in-salt electrolytes.[39] Indeed, the volume fractions ratios of modified POSS in TEG-based electrolytes, ε, are very large, ranging from 11.7% for the POSS-TFSI-25 sample up to 24.9% for the POSS-TFSI-10 sample (see Table 2). There are thus well-dispersed small aggregates at low content that progressively aggregates themselves upon an increase of ε. The same trend is observed when POSS are grafted by PEG chains for which ε reaches very large values (36.1% and 50.6%), even if steric repulsions between grafted chains prevent the formation of small aggregates in the case of POSS-TFSI-PEG$_{0.7}$-20 thanks to the high density of grafting. Schematic structures of all samples are proposed in Figure 2.

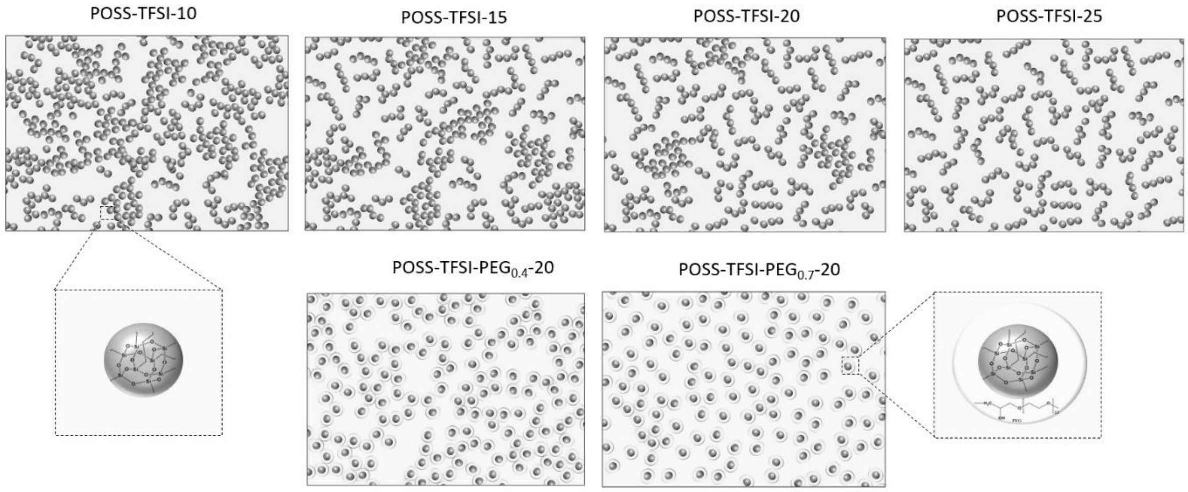

Figure 2. Schematic structure**s** for all electrolytes proposed thanks to SAXS results.

C-Thermal and thermodynamic properties of electrolytes

Thermo-gravimetric analyses have been performed from room temperature up to 600°C on pure TEG, TEG/LiTFSI complex (LiTFSI-20) as references, and the different POSS-TFSI-*y* and POSS-TFSI-PEG$_{x}$-*20* electrolytes. An isotherm at 100 °C during 1 hour has also been inserted in the thermal treatment. The thermograms are plotted in Figure 3a and 3b. The weight loss in isotherm condition is related to the saturation vapor pressure above the electrolyte which depends on the strength of the Li$^+$ salt-TEG interactions.[39] To fairly compare the different electrolytes, the weight loss was normalized by the TEG weight content (which depends on the charge of the anions and the PEG content). The values are listed in Table 3. For POSS-TFSI-*y* based electrolytes, the %wt loss decreases with y as expected, and tends to a plateau for y=OE/Li<15. For POSS-TFSI-PEG$_{x}$-*20* family, the weight loss is higher than with POSS-TFSI-*y* family, suggesting that the PEG shell reduced the strength of interaction of the macroanion with the surrounding TEG solvent. In particular, the POSS-TFSI-PEG$_{0,4}$-*20* with the highest PEG density presents even a higher weight loss relatively to pure TEG showing a reduction of the TEG---TEG interaction. That may due to the combination of high volume content (36.1 vol%) and limited interaction with the PEG shell in TEG. In addition, it strongly suggests that the Li^+ are preferentially complexed by the PEG shell (#8,5 Å according to SAXS analysis) than in the surrounding TEG.

After the isotherm, for each electrolyte, several degradation events are observed within the explored temperature range. In Figure 3a, the pure TEG evaporates/decomposes completely at 190 °C, while the mixture of TEG with LiTFSI salt (LiTFSI-20) exhibits two decomposition events, one around 210°C due to TEG and the other one slightly above 400°C (Figure 3b) due to the degradation of LiTFSI salt. All the POSS-TFSI-*y* electrolytes also present two decompositions process, one around 185°C (TEG) and another one around 270°C (POSS-TFSI) (Table 3 and Figure 3a). Interestingly, for POSS-TFSI-PEG$_x$-*20* electrolytes (Figure 3b), the PEG shell stabilizes the TFSI-POSS which decomposes at 310°C, while the degradation of the PEG occurs mostly above 350 °C.

We can thus estimate the composition of each electrolyte by using the derivative curve of the weight loss with temperature to precisely determine the boundary temperatures of each event for the weight integration. The obtained compositions have been added in Table 2. The values are very similar to the ones obtained by NMR analysis with a slight difference for the highly concentrated POSS-LiTFSI-y with y=10 and for the POSS-TFSI-PEG$_{0.4}$- 20.

Table 3. Thermal properties and stability of POSS based electrolytes obtained from DSC and TGA. The TEG and TEG-LiTFSI are given for reference.

Sample	Salts type	DSC					TGA	
		T_g (°C)	$T_{m\ peak}$ (°C)	ΔH_m (J/g)	ΔH_m (J/g TEG)	$\chi_{relative}$ (%)	Weight loss vs TEG content at 100 °C, 1h	$T_{d\ salt}$

							(%)	(°C)
TEG	--	-100[a]	-25	116.4	116.4	87.1	29.4	--
LiTFSI-20	Li-TFSI	-87	-34	43	54.1	40.5	5.4	409
POSS-TFSI-10	POSS-TFSI	-76	-31	11	17.6	13.1	18.3	270
POSS-TFSI-15		-77	-27	24	33.6	25.2	18.7	271
POSS-TFSI-20		-79	-26	45	58.7	43.9	20.1	269
POSS-TFSI-25		-81	-27	58	72.0	53.8	26.0	268
POSS-PEG$_{0.7}$-20	POSS-PEG$_{0.7}$	-87	-32; 1	12; 31	27.9	20.1	23.4	300; 380
POSS-PEG$_{0.4}$-20	POSS-PEG$_{0.4}$	-85	-27; -8	1;7	2.0	1.5	36.1	300; 360

[a]Glass transition temperature of pure TEG obtained from ref [48].

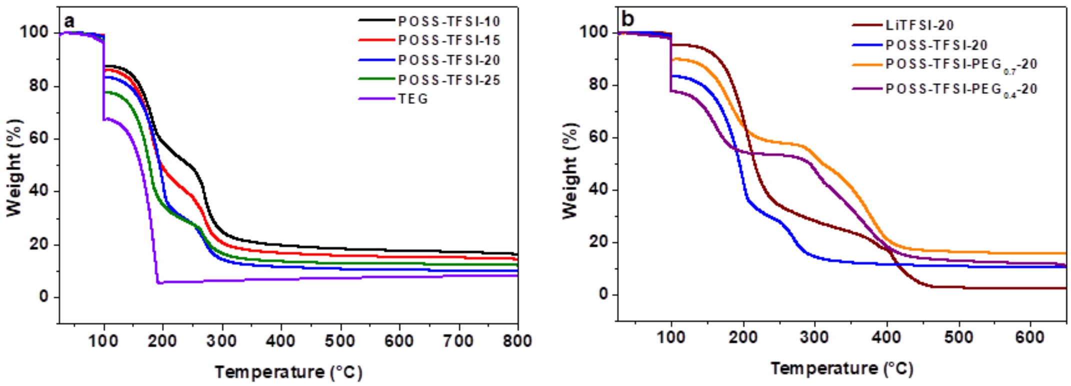

Figure 3. TGA curves as a function of POSS concentration (a) and type of POSS compared to LiTFSI at the same EO/Li ratio (b)~~.~~ TGA curves during isotherm can be found in Supporting Information (Figure S13).

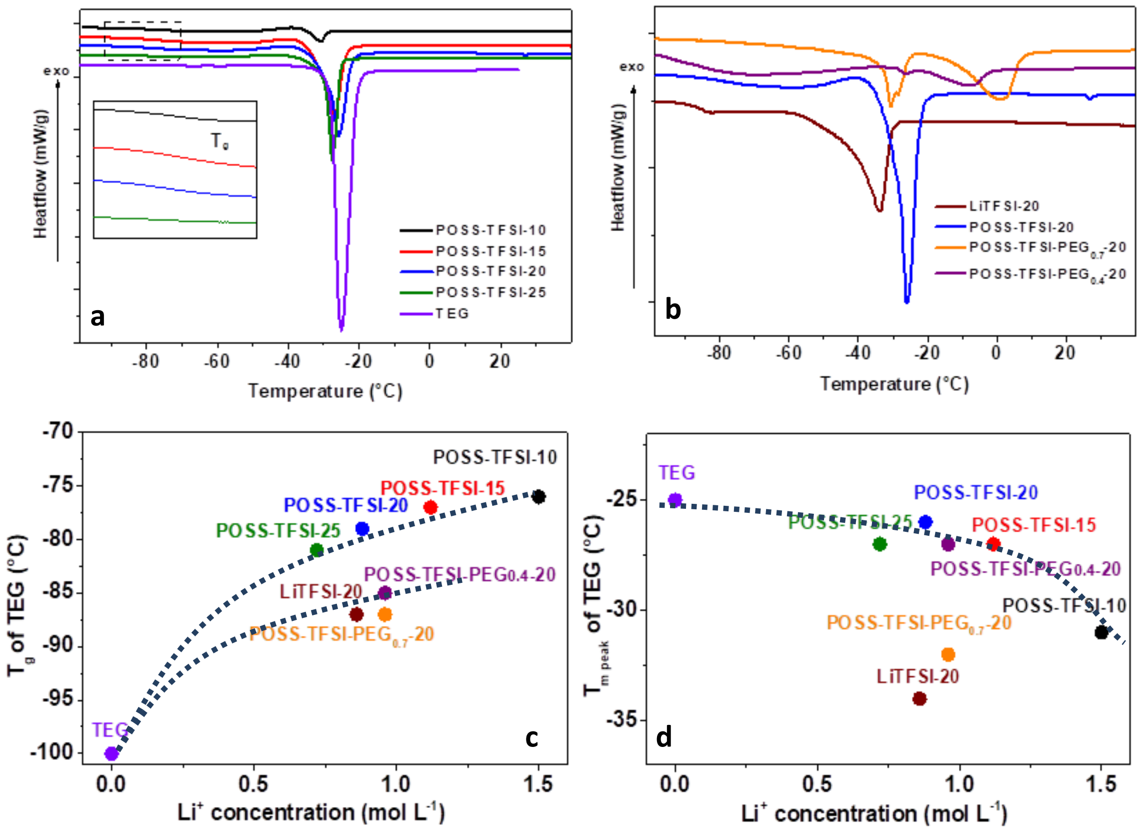

Figure 4. (a, b) DSC curves of the prepared electrolytes, (c) glass transition and (d) melting temperatures of POSS based electrolytes as a function of Li$^+$ concentration.

The DSC traces recorded during the second heating run of POSS-TFSI-*y* electrolytes at different EO/Li ratios and of neat TEG are presented in Figure 4a and are compared with LiTFSI-20 and POSS-TFSI-PEG$_x$-*20* at the same EO/Li ratio in Figure 4b. For the POSS-TFSI-*y* based electrolytes (Fig. 4a), the thermograms present a typical step at about -80 °C corresponding to the TEG glass transition temperature (T_g) and an endothermic peak typical of the TEG melting at about -30 °C (T_m).[39] Indeed, the DSC trace of the neat TEG presents a melting peak at a similar temperature while its T_g was observed in the literature at much lower temperature of -100 °C.[48] Interestingly, the POSS-TFSI-PEG$_x$-20 (Figure 4b) based electrolytes present two melting peaks on the DSC curves, a clear sign for phase separation at least partially, between the two oligo-ethers TEG and PEG. Accordingly, this effect is increased with the PEG shell density, from POSS-TFSI-PEG$_{0.4}$-20 to POSS-TFSI-PEG$_{0.7}$-20 the melting enthalpy of both TEG and PEG is increased. These results confirm the isothermal weight loss analysis in the previous part.

In Figure 4c, the T_g of the electrolyte are reported as a function of the salt concentration. The T_m, T_g, melting enthalpies and crystallinity degree for all the electrolytes are listed in Table 3. For POSS-TFSI-*y*, as expected the T_g increases with the salt content while T_m decreases due to TEG (Figure 4d) segments involved in binding with Li^+ cation.[49,50] In addition, compared to the LiTFSI-20 electrolyte, the POSS-TFSI-*y* based electrolytes present higher T_g despite their lower interaction with TEG observed by TGA while the T_g of the POSS-TFSI-PEG$_x$-*20* electrolytes are close to that of LiTFSI-20. These counterintuitive results can be explained by a different mechanism in POSS-based electrolytes. Unlike LiTFSI where the increase of T_g is mostly governed by the Li---TEG coordination, the glass transition temperature can be strongly affected by the volume occupied by POSS-based macroanions, similar to polymer nano-composite.[51] Indeed, the large size of POSS-anion (#11.5 Å for POSS-TFSI and #20 Å for POSS-TFSI-PEG$_x$ according to SAXS analysis), and thus the high volume content (from 11.7 to 50.5% in Table 2) of POSS-anion creates an important steric hindrance on TEG chain mobility. This effect compensates the lower interaction (dominated by the Li^+ solvation in TEG) between POSS-TFSI and POSS-TFSI-PEG$_x$ salts and TEG compared to LiTFSI, resulting in higher T_g and similar values, respectively.

D-Transport properties

The temperature dependence of the ionic conductivities of the POSS based electrolytes is plotted in Arrhenius coordinates in Figure 5a. The LiTFSI-20 reference electrolyte conductivity is more than one order of magnitude higher than the POSS-TFSI-y based electrolytes (around 10^{-4} S.cm^{-1} versus 3×10^{-3} S cm^{-1} at 25°C).[52] The POSS-TFSI-PEG$_x$-20 based electrolyte presents quite logically according to the previous analysis on the solvation, the lowest conductivity (around 3×10^{-5} S cm^{-1} at 25°C).

The conductivity curves in Figure 5a present a characteristic curvature of viscous electrolytes according to a Vogel–Tammann–Fulcher (VTF) type behavior[53] (Equation 8). The temperature dependence of the conductivity was fitted using the equation:[54–56]

$$\sigma(T) = \frac{\sigma_o}{\sqrt{T}} e^{\frac{-E_a}{R(T-T_o)}} \quad \text{(Equation 8)}$$

with the pre-exponential term σ_o proportional to the amount of ionic mobile charges, E_a a pseudo-activation energy, R the perfect gas constant, and T_o the ideal glass transition temperature.

The σ_o, E_a, and T_o parameters of the VTF equation were adjusted ($\chi^2 > 0.99$) to fit the experimental data. The results of the best fits are added as a continuous line in Figure 5 and the fitting parameters are presented as a function of C_{Li^+} in Figure S14. The $T_g - T_o$ difference is around of 40 K for the POSS-TFSI-y and LiTFSI-20 electrolytes, except for the highly concentrated POSS-TFSI-10 where this value is 25 K, which is still in agreement with the physical basis of the VTF model supported by the free volume theory.[45,53] As expected, the pre-exponential term σ_o increases proportionally with Li$^+$ concentration. Moreover, for all systems, a similar "pseudo" activation energy around 6.5 kJ mol^{-1} is obtained suggesting the same transport mechanism mainly driven by the segmental motions of TEG.[57]

To go further, we plot in Figure 5b the conductivity as a function of the reduced temperature (T-T$_o$) in Arrhenius coordinates. In this representation, the reduced conductivity forms parallel straight lines. It also provides a comparison of the conductivity of the electrolytes at the same temperature distance from their respective T_g[58] which mainly reflects the concentration of free charge carriers as the free volume is similar. In this representation, the gradation of conductivity of the POSS-TFSI-y electrolytes as a function of the salt concentration is clear. Interestingly, for the same Li^+ concentration, the reduced conductivities of POSS-TFSI-20 and POSS-TFSI-PEG_x-20 electrolytes are 10 and 50 times lower than the reference LiTFSI-20 electrolyte whatever the temperature, respectively. This important difference may be attributed in part to the decrease of the neat anionic flux thanks to the viscous hindrance on the large POSS based macroanions, resulting in an increase of the Li^+ transport number in these electrolytes. Another part can be attributed to a limited dissociation (and solvation) of Li^+ salt by the TEG solvent in POSS based electrolytes compared to LiTFSI-20 reference electrolyte, which is supported by the TGA/DSC analyses on salt-TEG interaction.

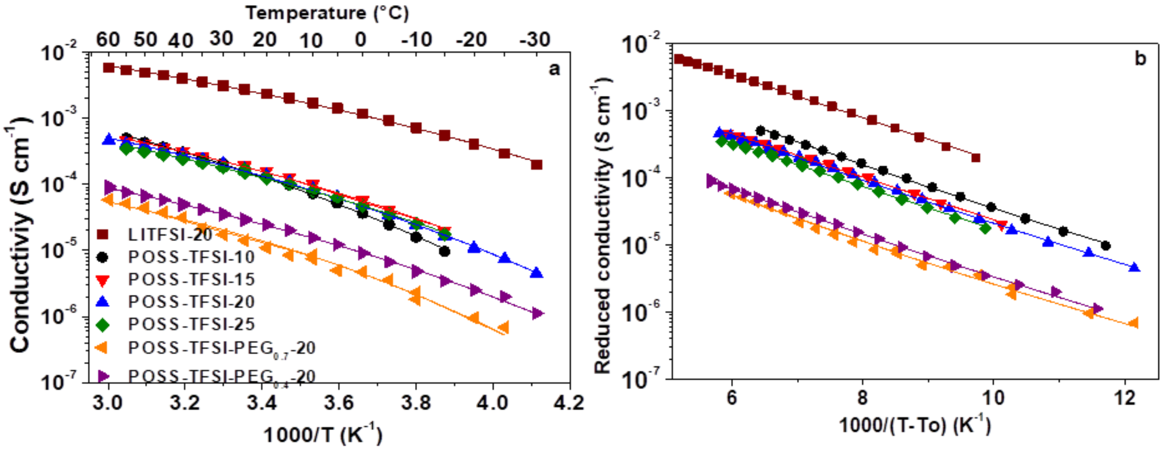

Figure 5. Conductivity as a function of temperature for all the electrolytes (a) with corresponding reduced conductivity obtained from VTF fitting (b). Measured values presented as markers and fitting values as continuous line.

Especially, the addition of PEG within the POSS (POSS-TFSI-PEG$_x$-*20*) results in a partial phase separation according to the DSC between the PEG shell and the TEG matrix, which translates in a sharp decrease of ionic conductivity of one order of magnitude together with low values of glass transition temperature (see Figure 5b). Indeed, most part of the Li^+ ions is probably trapped in the PEG shell, and thus, not solvated by the continuous TEG matrix.

To better separate the transport dynamics to the Li^+ solvation chemical equilibrium, PFG-NMR was used to measure at 60°C for all the studied electrolytes, the self-diffusion coefficient of ^7Li (cation), ^{19}F (anion) and ^1H (solvent (TEG) and PEG (POSS shell)). The values are reported in Table 4. Interestingly, the TFSI anion and solvent diffusion coefficients are similar in LiTFSI-20 while the POSS-anion diffusion coefficient is nearly twenty (POSS-TFSI-y) to fifty (POSS-TFSI-PEG$_x$-20) times lower than the solvent diffusion coefficient confirming the strong slowdown of this macroanion due to viscous hindrance thanks to their size. Moreover, for POSS-TFSI-PEG$_x$ based electrolytes, two distributions of H diffusion were registered corresponding to the high mobility of CH_2 in TEG (solvent) and the low mobility of PEG grafted on POSS molecules, respectively. One can notice that the PEG population diffuses at a similar rate than the macro-anions they are grafted on. In addition, the ratio of these two distributions is proportional to the molar ratio and allows us to estimate the composition of these POSS-TFSI-PEG$_x$-20 electrolytes: 52 wt% and 39 wt% of PEG in POSS-TFSI-PEG$_x$ for x equal 0.7 and 0.4, respectively. These values are similar to those obtained by chemical NMR and listed in Table 2, which strongly support our interpretation.

In addition, conductivity (σ_{NE}) of the electrolytes can be calculated thanks to the Nernst-Einstein equation using the diffusion coefficients of the lithium cation (D_{Li}) and fluorine anion (D_F) derived from the PFG-NMR and the salt concentration listed in Table 2:

$$\sigma_{NE} = \frac{F^2}{RT} \sum (C_+ z_+{}^2 D_{Li} + C_- z_-{}^2 D_F) \text{ (Equation 9)}$$

where F is the Faraday's constant, C_+ and $C_- = C_+ \times \frac{z_+}{z_-}$ are the concentrations of cations and anions in the electrolyte, and, z_+ (= 1) and z_- are the valence of the cation (Li^+) and anions (see Table 2), respectively.

The values of the Haven's ratio[59,60] between experimentally measured conductivities thanks to EIS, σ_{EIS}, and the calculated Nernst-Einstein conductivities, σ_{NE}, at a given temperature, are listed in Table 4 and are presented in Figure 6 as a function of Li^+ concentration. This ratio is classically used as a metric for Lithium dissociation rate α.[61,62] Similarly to the conductivity, three families can be observed depending on the nature of the anion, the highest dissociation coefficient α is obtained with LiTFSI-20, while for POSS-TFSI-*y* it is reduced by a factor 2 to 3 and by a factor 6 to 8 for POSS-TFSI-PEG$_x$-*20.* This gradation is in accordance with the expected behavior suggested by TGA/DSC and conductivity analyses. It confirms that the grafting of the PEG traps most of the Li^+ ion in the PEG shell, reducing the free Li^+ ion. In the case of POSS-TFSI-y, the reduced value of alpha can be due to the high anionic charge density on the POSS core that limits the dissociation rate. Concerning LiTFSI based electrolyte, despite the fact that diffusion coefficients obtained from our measurements are slightly higher than the literature,[63] similar Heaven ratio have been found.

Table 4. Diffusion coefficients measured by PFG-NMR at 60°C and electrolyte conductivities at 60°C measured by EIS and calculated by Nernst-Einstein (Equation 9), Haven's ratios σ_{EIS}/σ_{NE}, and, finally Li^+ transport number determined by both electrochemical and NMR methods as a function of salt nature and content.

Samples	Filler charge		Diffusion coefficient at 60 °C ($\times 10^{-11}$ m^2 s^{-1})			Conductivity at 60 °C (S cm^{-1})		Haven ratio	σ_o	Li^+ transport number	
	z_+	z_-	^1H	^{19}F	^7Li	*	Nernst-Einstein	(α)		t^+_{NMR}	$t^+_{El.}$
LiTFSI-20	1	1	31.0	28.8	20.0	6.1×10^{-3}	1.4×10^{-2}	0.43	6.21	0.4	0.27
POSS-TFSI-10	1	10	6.4	0.4	1.7	5.9×10^{-4}	2.4×10^{-3}	0.22	1.35	0.69	0.71
POSS-TFSI-15	1	10	12.0	0.8	2.1	5.4×10^{-4}	3.8×10^{-3}	0.14	0.85	0.64	0.8
POSS-TFSI-20	1	10	12.0	0.7	2.1	4.5×10^{-4}	2.3×10^{-3}	0.17	0.79	0.64	0.72
POSS-TFSI-25	1	10	11.0	0.9	2.3	4.1×10^{-4}	2.1×10^{-3}	0.15	0.61	0.63	0.75
POSS-TFSI-$PEG_{0.7}$-20	1	8	13.0 (62%) 0.3 (40%)	0.2	1.3	5.3×10^{-5}	1.1×10^{-3}	0.05	0.10	0.93	0.86
POSS-TFSI-$PEG_{0.4}$-20	1	7	17.0 (76%) 0.4 (26%)	0.4	1.7	8.3×10^{-5}	1.3×10^{-3}	0.06	0.12	0.91	0.77

* values at 60° C are calculated from VTF fitting of conductivity presented in Figure 5.

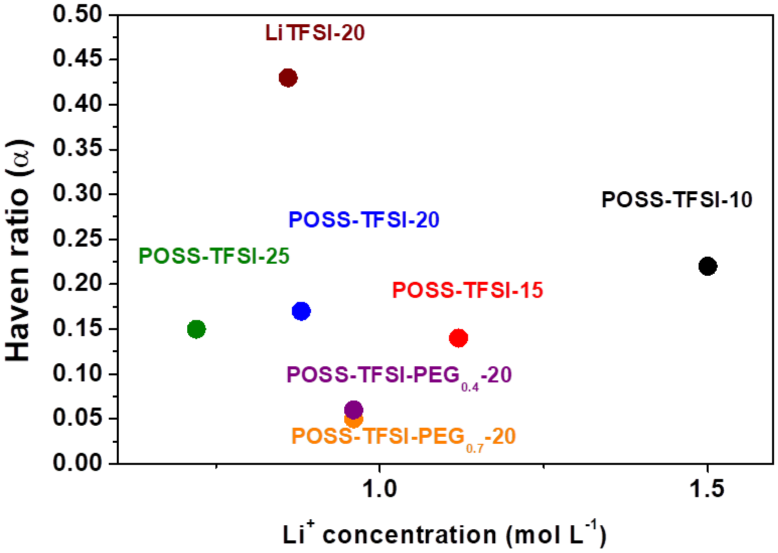

Figure 6. Haven's ratio as a function of concentration for all studied electrolytes.

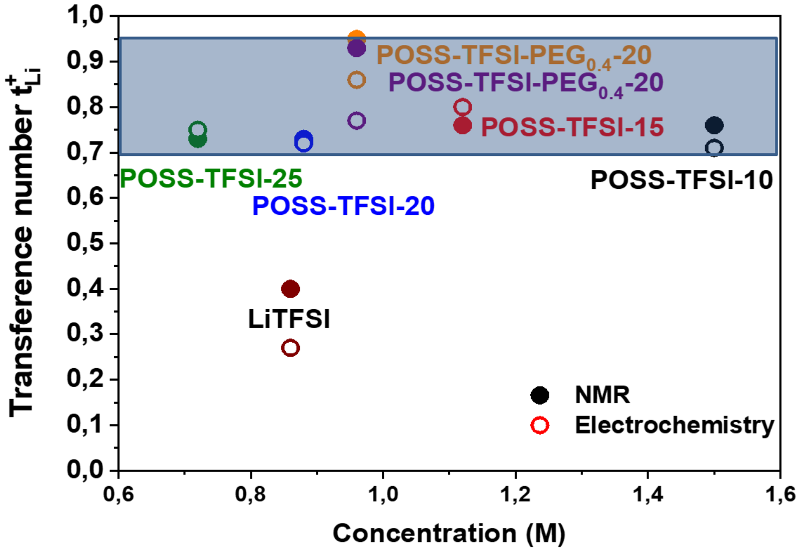

Figure 7. Transference number as a function of Li^+ concentration obtained from both electrochemical and NMR methods: comparison between macro-anions and TFSI.

Finally, the last factor that governs the transport properties in classical electrolyte is the Li^+ transference number. It was measured by two independent methods including electrochemistry (t^+_{El}) and PFG-NMR (t^+_{NMR}). It is worth noticing that the dissociation rate α of lithium previously determined influences both the concentration of conducting species and for the multi-anions, their charge values (C_+, C_- and z_- in Equation 4). Therefore, Equation 4 of t^+_{NMR} should be modified taking the dissociation rate α into account according to:

$$t^+_{NMR} = \frac{\sigma_+}{\sigma_+ + \sigma_-} = \frac{D_+}{D_+ + \alpha z_- D_-} \text{(Equation 10)}$$

The transference number values calculated from Equation 10 (t^+_{NMR}) and determined by electrochemical method (t^+_{El}) are presented in Figure 7 as a function of $C_{Li}{}^+$ and are added in Table 4. The value of 0.43 for the LiTFSI-20 electrolyte determined by NMR is in accordance with literature value.[64] Regardless of POSS concentration and measuring methods, our electrolytes exhibit a t^+ of 0.7-0.8 for POSS-TFSI-*y* and above 0.85 for POSS-TFSI-PEG$_x$-*20*, two times higher than LiTFSI based electrolyte. These values are also in good agreement with other POSS based electrolytes reported in the literature.[36,39]

E-Transport equation and lithium cation conductivity

From the previous parts, it has been shown that the lower conductivity of POSS-based electrolytes finds its foundation in different physico-chemical factors such as i) an increase of the electrolytes glass transition temperature T_g (Table 3, Figure 4b), which probes the electrolyte viscosity, mainly due to the large volume proportion ε (up to 50vol%) of POSS macro-anions that leads to the formation of linear or ramified aggregates (Figure 2) similar to the nanocomposite effect, ii) a lower dissociation rate α (Table 4, Figure 6) that depends on the charge density (POSS-TFSI) and the affinity of the other monomer, herein PEG, grafted on the POSS (POSS-TFSI-PEG$_x$) with the solvent, iii) an expected reduction of the anionic mobility relatively to the Li^+ that leads to a strong increase of its transference number, t^+ (Table 4, Figure 7). Finally, another factor as to be taken into account, *i.e.* iv) the topologic hindrance to the cationic flux due to the large volume occupied by the (very) less mobile POSS-anion, acting as nanofillers, which translates in a tortuosity factor, τ.[65,66]

Therefore, now we have in hands a manual to fully compare the "true" Li^+ ionic conductivity, σ_{Li+} of the different electrolytes in order to draw the path to the design of efficient macro-anions based on physico-chemical considerations. Indeed, σ_{Li+} can be calculated by applying to σ all the factors previously determined: T_g (account the viscosity of the electrolyte), t^+ (eliminate the conductivity of anion), α (account for mobile dissociated Li^+), ε (the volume fraction of macro-anion acting as nanofillers, $(1-\varepsilon)$ being the volume fraction of the continuous liquid electrolyte phase), and the tortuosity factor τ according to Equation 11:

$$\sigma_{Li^+}^{(T-T_g)} = \frac{\sigma^{(T-T_g)} \times t_{El.}^{+} \times \tau}{\alpha \times (1-\varepsilon)} \text{ (Equation 11)}$$

where $\sigma^{\text{(T-Tg)}}$ is the experimentally measured conductivity at a certain distance of the T_g of a given electrolyte (reduced conductivity), $\sigma_{Li^+}^{T-T_g}$ is the "true" Li^+ conductivity.

In these dispersions of anionic nanofillers, as a first approximation for their tortuosity, we can use the equation 12 firstly derived by Weissberg,[66] and proposed by Comity and Renaud[67] for the dispersion of non-porous spheres. The validity of equation 12 has been previously demonstrated thanks to conductivity measurements[65] on a dispersion of silica spheres in an aqueous electrolyte.

$\tau=1-0.49\times\ln(1-\varepsilon)$ (Equation 12)

It is worth noticing, that in case of the reference LiTFSI-20 electrolyte, ε is zero and τ is equal to unity.

As an example of the application of eq. 11, the separated impact of each previously defined parameters ($\tau/(1-\varepsilon)$, α and t^+) on the reduced Li^+ conductivity $\sigma_{Li^+}^{T-T_g}$, is shown in Figure 8a for the case of POSS-TFSI-$PEG_{0.7}$-20.

Then the "true" reduced Li^+ conductivities $\sigma_{Li^+}^{T-T_g}$ calculated thanks to Equation 11 (and 12) using the values in Table 2 and Table 4 for the parameters ($\sigma^{\text{(T-Tg)}}$, t^+, α, ε and τ) experimentally and independently measured, are plotted in Arrhenius coordinates in Figure 8b for the different types of electrolyte. By removing all mentioned factors, the reduced Li^+ conductivities of all types of electrolyte- reference LiTFSI-20 electrolyte as well as both types of POSS-based electrolytes (either POSS-TFSI-20 or POSS-TFSI-PEG_x-20), are almost over-imposed, while the conductivity $\sigma^{\text{(T-Tg)}}$ itself (see Figure 5) varies of almost two orders of magnitude according to the structure of the anion. These results demonstrate that the Equation 11 captures correctly the physical origin of the conductivity variations from one anion to the other. In addition, several others properties can be deduced thanks to the validity of the equation 11. For instance, the increase of Li$^+$ concentration results, in a very good accordance with the physical expectation, in a quasi linear increase with a slope of one of σ_{Li+} as shown in Figure 8c. Therefore, from this fundamental study on transport properties of original macro-anions based on a POSS core, we can deduce some principles for the design of such anions.

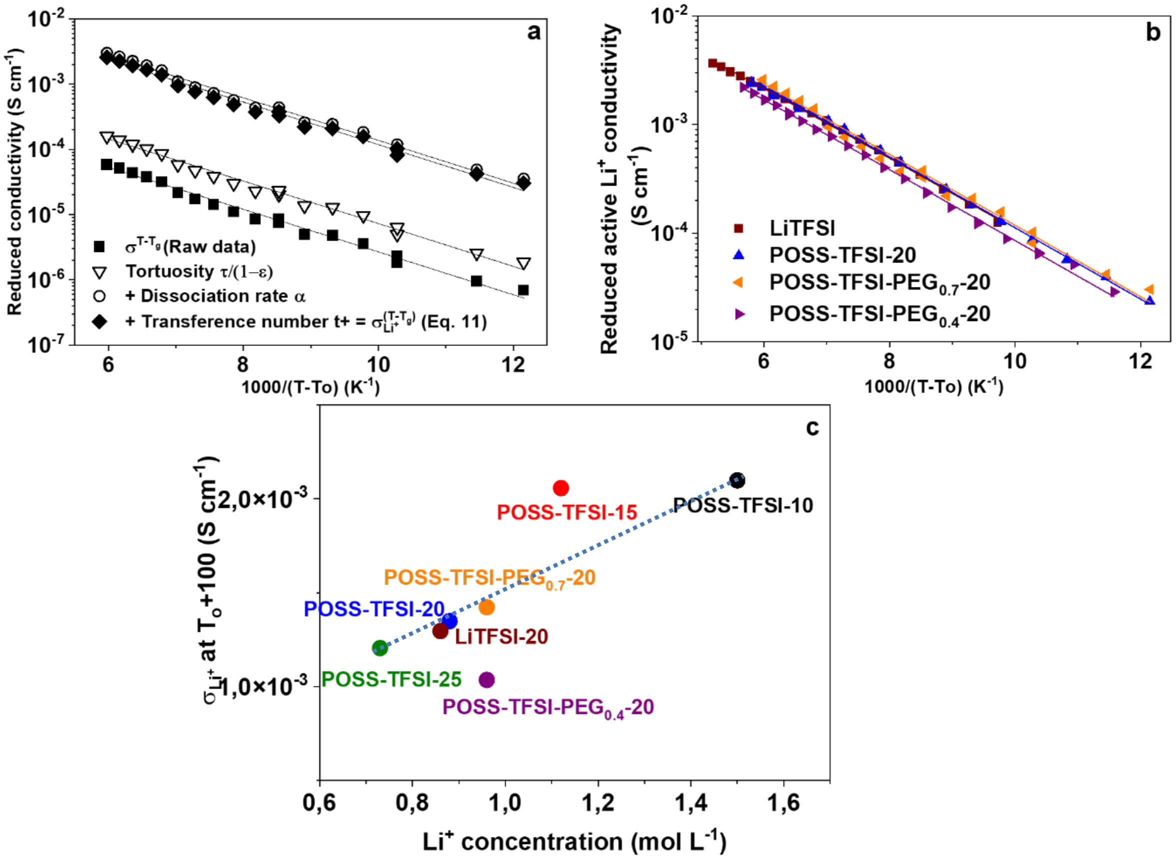

Figure 8. a) Evolution of Li$^+$ reduced conductivity of POSS-TFSI-PEG$_{0.7}$-20 corrected by the tortuosity, dissociation rate, and transference number t$^+$ thanks to eq. 11 (and 12) ; b) The “true” reduced Li$^+$ conductivity compared for the different TEG based electrolytes calculated according to Equation 11, using parameters measured experimentally and listed in Table 2 and Table 4; c) “True” Li$^+$ conductivity at the same distance to the glass transition temperature (T$_o$+100) as a function of Li$^+$ concentration.

CONCLUSION

Two families of lithium bulky salts were developed based on hybrid macro-anion concepts (POSS-TFSI and POSS-TFSI-PEG) as a new route to develop electrolytes with high Li^+ transport number. Indeed, the best TEG-based electrolytes (POSS-TFSI-15) exhibit satisfactory conductivity at room temperature of 1.86×10^{-4} S cm^{-1} combining high transference number above 0.75, which is very promising for battery application.

Moreover, the combination of SAXS, DSC/TGA, PFG-NMR and EIS allows us to propose and effective model of the transport properties for these electrolytes (equation 11) considering the effect of the macro-anion impact on the molecular dynamics (T_g), the Li^+ transport number (t^+), the dissociation rate (α) and the tortuosity factor (τ).

From that model, it can be drawn some principles for the design of macro-anions: There is a compromise to be found between increasing the size of the anion which pilots the anion dynamics (t^+), and its impact on the macroscopic electrolyte properties such as an increase of both the matrix viscosity (increasing T_g, nanocomposite effect), and the tortuosity factor, τ.

Another trade off, is the strength of the macro-anion affinity with the solvent that impedes strongly the T_g values: the less affinity the lowest the impact on T_g. For example, the length and the nature of end function of ether grafted monomer could play a strong role on controlling that parameter. In addition, solvent macro-anion affinity with the solvent drives also the dissociation rate which depends also on the anion (charge) density carried out by the POSS core.

Equation 11 can be used as a manual for optimizing the design of anion to improve electrolytes transport properties.

ASSOCIATED CONTENT

Supporting Information The data for the preparation of liquid electrolytes (Table S1); synthesis route of POSS-TFSI and POSS-TFSI-PEG compounds (Scheme S1); ^{1}H, ^{19}F and ^{7}Li NMR spectra of all synthesized products (Figures S3 – S10); comparison of measured density with those of ideal mixtures (Figure S11) and supplement data on SAXS, TGA, conductivity and transport number measurements (Figures S1 - S2 and Figures S12 – S14).

AUTHOR INFORMATION

Corresponding Author

*T. N. T. Phan, trang.phan@univ-amu.fr, R. Bouchet, Renaud.bouchet@lepmi.grenoble-inp.fr

Present Addresses

†Current address: CY Cergy Paris Université, LPPI, F-95000 Cergy, France

Author Contributions

TNTP synthesized the POSS macro anions, FC and SM carried out the SAXS analyses, FZ, SV and PS carried out the PFG-NMR experiments, TKLN makes the calorimetric, thermal and electrochemical measures. TKLN and RB analyzed the transport properties. RB and TNTP supervised the project. The manuscript was written through contributions of all authors. All authors have given approval to the final version of the manuscript.

Funding Sources

ACKNOWLEDGEMENTS

We thank the French Agence Nationale de la Recherche (ANR) for the funding of the project SELPHy, N° ANR-17 CE05-0032-01.

REFERENCES

(1) PNNL: News - Battery500 consortium to spark EV innovations https://www.pnnl.gov/news/release.aspx?id=4295 (accessed 2019 -07 -02).

(2) Xu, W.; Wang, J.; Ding, F.; Chen, X.; Nasybulin, E.; Zhang, Y.; Zhang, J.-G. Lithium Metal Anodes for Rechargeable Batteries. *Energy Environ. Sci.* **2014**, *7* (2), 513–537. https://doi.org/10.1039/C3EE40795K.

(3) Chazalviel, J.-N. N. Electrochemical Aspects of the Generation of Ramified Metallic Electrodeposits. *Phys. Rev. A* **1990**, *42* (12), 7355–7367. https://doi.org/10.1103/PhysRevA.42.7355.

(4) Monroe, C.; Newman, J. Dendrite Growth in Lithium/Polymer Systems. *J. Electrochem. Soc.* **2003**, *150* (10), A1377. https://doi.org/10.1149/1.1606686.

(5) Frenck, L.; Sethi, G. K.; Maslyn, J. A.; Balsara, N. P. Factors That Control the Formation of Dendrites and Other Morphologies on Lithium Metal Anodes. *Front. Energy Res.* **2019**, *7*, 115. https://doi.org/10.3389/fenrg.2019.00115.

(6) Tikekar, M. D.; Choudhury, S.; Tu, Z.; Archer, L. A. Design Principles for Electrolytes and Interfaces for Stable Lithium-Metal Batteries. *Nat. Energy* **2016**, *1* (9), 1–7. https://doi.org/10.1038/nenergy.2016.114.

(7) Liu, H.; Cheng, X. B.; Huang, J. Q.; Yuan, H.; Lu, Y.; Yan, C.; Zhu, G. L.; Xu, R.; Zhao, C. Z.; Hou, L. P.; He, C.; Kaskel, S.; Zhang, Q. Controlling Dendrite Growth in Solid-State Electrolytes. *ACS Energy Lett.* **2020**, *5* (3), 833–843. https://doi.org/10.1021/acsenergylett.9b02660.

(8) Shishvan, S. S.; Fleck, N. A.; McMeeking, R. M.; Deshpande, V. S. Dendrites as Climbing Dislocations in Ceramic Electrolytes: Initiation of Growth. *J. Power Sources* **2020**, *456*, 378–7753. https://doi.org/10.1016/j.jpowsour.2020.227989.

(9) Golozar, M.; Paolella, A.; Demers, H.; Savoie, S.; Girard, G.; Delaporte, N.; Gauvin, R.; Guerfi, A.; Lorrmann, H.; Zaghib, K. Direct Observation of Lithium Metal Dendrites with Ceramic Solid Electrolyte. *Sci. Rep.* **2020**, *10* (1), 18410. https://doi.org/10.1038/s41598-020-75456-0.

(10) Bouchet, R.; Maria, S.; Meziane, R.; Aboulaich, A.; Lienafa, L.; Bonnet, J.-P. P.; Phan, T. N. T.; Bertin, D.; Gigmes, D.; Devaux, D.; Denoyel, R.; Armand, M. Single-Ion BAB Triblock Copolymers as Highly Efficient Electrolytes for Lithium-Metal Batteries. *Nat. Mater.* **2013**, *12* (5), 452–457. https://doi.org/10.1038/nmat3602.

(11) Galvin, M. E.; Mayes, A. M.; Sadoway, D. R.; Kurian, M.; Trapa, P. E. Single-Ion Conducting Polymer–Silicate Nanocomposite Electrolytes for Lithium Battery Applications. *Electrochim. Acta* **2004**, *50* (10), 2125–2134. https://doi.org/10.1016/j.electacta.2004.09.020.

(12) Porcarelli, L.; Shaplov, A. S.; Bella, F.; Nair, J. R.; Mecerreyes, D.; Gerbaldi, C. Single-Ion Conducting Polymer Electrolytes for Lithium Metal Polymer Batteries That Operate at Ambient Temperature. *ACS Energy Lett.* **2016**, *1* (4), 678–682. https://doi.org/10.1021/acsenergylett.6b00216.

(13) Wong, D. H. C.; Thelen, J. L.; Fu, Y.; Devaux, D.; Pandya, A. A.; Battaglia, V. S.; Balsara, N. P.; DeSimone, J. M. Nonflammable Perfluoropolyether-Based Electrolytes for Lithium Batteries. *Proc. Natl. Acad. Sci. U. S. A.* **2014**, *111* (9), 3327–3331.

https://doi.org/10.1073/pnas.1314615111.

(14) Henderson, W. A.; Brooks, N. R.; Young, V. G. Tetraglyme-Li+ Cation Solvate Structures: Models for Amorphous Concentrated Liquid and Polymer Electrolytes (II). *Chem. Mater.* **2003**, *15* (24), 4685–4690. https://doi.org/10.1021/cm034352r.

(15) Zhang, H.; Han, H.; Cheng, X.; Zheng, L.; Cheng, P.; Feng, W.; Nie, J.; Armand, M.; Huang, X.; Zhou, Z. Lithium Salt with a Super-Delocalized Perfluorinated Sulfonimide Anion as Conducting Salt for Lithium-Ion Cells: Physicochemical and Electrochemical Properties. *J. Power Sources* **2015**, *296*, 142–149. https://doi.org/10.1016/j.jpowsour.2015.07.026.

(16) Qiao, L.; Cui, Z.; Chen, B.; Xu, G.; Zhang, Z.; Ma, J.; Du, H.; Liu, X.; Huang, S.; Tang, K.; Dong, S.; Zhou, X.; Cui, G. A Promising Bulky Anion Based Lithium Borate Salt for Lithium Metal Batteries. *Chem. Sci.* **2018**, *9* (14), 3451–3458. https://doi.org/10.1039/c8sc00041g.

(17) Ue, M.; Fujii, T.; Zhou, Z. Bin; Takeda, M.; Kinoshita, S. Electrochemical Properties of Li[CnF2n+1BF 3] as Electrolyte Salts for Lithium-Ion Cells. *Solid State Ionics* **2006**, *177* (3–4), 323–331. https://doi.org/10.1016/j.ssi.2005.10.023.

(18) Gładka, D.; Krajewski, M.; Młynarska, S.; Galińska, J.; Zygadło-Monikowska, E. Synthesis and Properties of New Carboxyborate Lithium Salts as Electrolytes for Lithium-Ion Batteries. *Electrochim. Acta* **2017**, *245*, 625–633. https://doi.org/10.1016/j.electacta.2017.05.170.

(19) Geiculescu, O. E.; Rajagopal, R.; Creager, S. E.; DesMarteau, D. D.; Zhang, X.; Fedkiw,

P. Transport Properties of Solid Polymer Electrolytes Prepared from Oligomeric Fluorosulfonimide Lithium Salts Dissolved in High Molecular Weight Poly(Ethylene Oxide). *J. Phys. Chem. B* **2006**, *110* (46), 23130–23135. https://doi.org/10.1021/jp062648p.

(20) Trzeciak, T.; Niedzicki, L.; Groszek, G.; Wieczorek, P.; Marcinek, M.; Wieczorek, W. New Trivalent Imidazole-Derived Salt for Lithium-Ion Cell Electrolyte. *J. Power Sources* **2014**, *252*, 229–234. https://doi.org/10.1016/j.jpowsour.2013.12.018.

(21) Buss, H. G.; Chan, S. Y.; Lynd, N. A.; McCloskey, B. D. Nonaqueous Polyelectrolyte Solutions as Liquid Electrolytes with High Lithium Ion Transference Number and Conductivity. *ACS Energy Lett.* **2017**, *2* (2), 481–487. https://doi.org/10.1021/acsenergylett.6b00724.

(22) Zhang, H.; Zhang, X.; Shiue, E.; Fedkiw, P. S. Single-Ion Conductors for Lithium Batteries via Silica Surface Modification. *J. Power Sources* **2008**, *177*, 561–565. https://doi.org/10.1016/j.jpowsour.2007.11.064.

(23) Schaefer, J. L.; Yanga, D. A.; Archer, L. A. High Lithium Transference Number Electrolytes via Creation of 3-Dimensional, Charged, Nanoporous Networks from Dense Functionalized Nanoparticle Composites. *Chem. Mater* **2013**, *25*, 839. https://doi.org/10.1021/cm303091j.

(24) Zhang, X.-W.; Fedkiw, P. S. Ionic Transport and Interfacial Stability of Sulfonate-Modified Fumed Silicas as Nanocomposite Electrolytes. *J. Electrochem. Soc.* **2005**, *152* (12), A2413. https://doi.org/10.1149/1.2109661.

(25) Lan, Z.; Chen, X.; Zhang, X.; Zhu, C.; Yu, Y.; Wei, J. Transparent, High Glass-Transition Temperature, Shape Memory Hybrid Polyimides Based on Polyhedral Oligomeric Silsesquioxane. *Polymers (Basel).* **2019**, *11* (6), 1–11. https://doi.org/10.3390/POLYM11061058.

(26) Polu, A. R.; Rhee, H. W. Nanocomposite Solid Polymer Electrolytes Based on Poly(Ethylene Oxide)/POSS-PEG (N=13.3) Hybrid Nanoparticles for Lithium Ion Batteries. *J. Ind. Eng. Chem.* **2015**, *31*, 323–329. https://doi.org/10.1016/j.jiec.2015.07.005.

(27) Reddy Polu, A.; Rhee, H.-W.; Jeevan, M.; Reddy, K.; Shanmugharaj, A. M.; Ryu, S. H.; Kim, D. K.; Rhee, H.-W. Effect of POSS-PEG Hybrid Nanoparticles on Cycling Performance of Polyether-LiDFOB Based Solid Polymer Electrolytes for All Solid-State Li-Ion Battery Applications. *J. Ind. Eng. Chem.* **2017**, *45*, 68–77. https://doi.org/10.1016/j.jiec.2016.09.004.

(28) Ma, J.; Zhang, M.; Luo, C.; Li, M.; Guan, X.; Chen, F.; Ma, X. Polyethylene Glycol Functionalized Polyhedral Cage Silsesquioxane as All Solid-State Polymer Electrolyte for Lithium Metal Batteries. *Solid State Ionics* **2021**, *363*, 167–2738. https://doi.org/10.1016/j.ssi.2021.115606.

(29) Kim, S. K.; Kim, D. G.; Lee, A.; Sohn, H. S.; Wie, J. J.; Nguyen, N. A.; MacKay, M. E.; Lee, J. C. Organic/Inorganic Hybrid Block Copolymer Electrolytes with Nanoscale Ion-Conducting Channels for Lithium Ion Batteries. *Macromolecules* **2012**, *45* (23), 9347–9356. https://doi.org/10.1021/ma301404q.

(30) Kim, D.-G.; Shim, J.; Hong Lee, J.; Kwon, S.-J.; Baik, J.-H.; Lee, J.-C. Preparation of

Solid-State Composite Electrolytes Based on Organic/ Inorganic Hybrid Star-Shaped Polymer and PEG-Functionalized POSS for All-Solid-State Lithium Battery Applications. *Polymer (Guildf).* **2013**, *54*, 5812–5820. https://doi.org/10.1016/j.polymer.2013.08.049.

(31) Cao, P. F.; Wojnarowska, Z.; Hong, T.; Carroll, B.; Li, B.; Feng, H.; Parsons, L.; Wang, W.; Lokitz, B. S.; Cheng, S.; Bocharova, V.; Sokolov, A. P.; Saito, T. A Star-Shaped Single Lithium-Ion Conducting Copolymer by Grafting a POSS Nanoparticle. *Polymer (Guildf).* **2017**, *124*, 117–127. https://doi.org/10.1016/j.polymer.2017.07.052.

(32) Boaretto, N.; Bittner, A.; Brinkmann, C.; Olsowski, B.-E.; Schulz, J.; Seyfried, M.; Vezzù, K.; Popall, M.; Noto, V. Di. Highly Conducting 3D-Hybrid Polymer Electrolytes for Lithium Batteries Based on Siloxane Networks and Cross-Linked Organic Polar Interphases. *Chem. Mater* **2014**, *26*, 22. https://doi.org/10.1021/cm5024647.

(33) Lee, J. Y.; Lee, Y. M.; Bhattacharya, B.; Nho, Y. C.; Park, J. K. Solid Polymer Electrolytes Based on Crosslinkable Polyoctahedral Silsesquioxanes (POSS) for Room Temperature Lithium Polymer Batteries. *J. Solid State Electrochem.* **2010**, *14* (8), 1445–1449. https://doi.org/10.1007/s10008-009-0968-1.

(34) Chinnam, P. R.; Zhang, H.; Wunder, S. L. Blends of Pegylated Polyoctahedralsilsesquioxanes (POSS-PEG) and Methyl Cellulose as Solid Polymer Electrolytes for Lithium Batteries. *Electrochim. Acta* **2015**, *170*, 191–201. https://doi.org/10.1016/j.electacta.2015.04.010.

(35) Zhang, X.; Liu, S.; Yin, J. Modified Sulfonated Poly(Arylene Ether Sulfone)-b-Polybutadiene (SPAES-b-PB) Membrane for Fuel Cell Applications. *J. Memb. Sci.* **2006**, *275* (1–2), 119–126. https://doi.org/10.1016/j.memsci.2005.09.011.

(36) Chinnam, P. R.; Wunder, S. L. Polyoctahedral Silsesquioxane-Nanoparticle Electrolytes for Lithium Batteries: POSS-Lithium Salts and POSS-PEGs. *Chem. Mater.* **2011**, *23* (23), 5111–5121. https://doi.org/10.1021/cm2015675.

(37) Chinnam, P. R.; Wunder, S. L. Self-Assembled Janus-like Multi-Ionic Lithium Salts Form Nano-Structured Solid Polymer Electrolytes with High Ionic Conductivity and Li+ Ion Transference Number. *J. Mater. Chem. A* **2013**, *1* (5), 1731–1739. https://doi.org/10.1039/c2ta00085g.

(38) Yang, G.; Chanthad, C.; Oh, H.; Ayhan, I. A.; Wang, Q. Organic-Inorganic Hybrid Electrolytes from Ionic Liquid-Functionalized Octasilsesquioxane for Lithium Metal Batteries. *J. Mater. Chem. A* **2017**, *5* (34), 18012–18019. https://doi.org/10.1039/c7ta04599a.

(39) Chereddy, S.; Chinnam, P. R.; Chatare, V.; Diluzio, S. P.; Gobet, M. P.; Greenbaum, S. G.; Wunder, S. L. An Alternative Route to Single Ion Conductivity Using Multi-Ionic Salts. *Mater. Horizons* **2018**, *5* (3), 461–473. https://doi.org/10.1039/c7mh01130j.

(40) Wunder, S. L.; Chinnam, P. R. Multi-Ionic Salts and Used Therof. US 2018/0355116 A1, 2020.

(41) Glé, D.; Phan, T. N. T.; Monier, V.; Charles, L.; Bertin, D.; Gigmes, D. Synthesis and Characterization of Polyhedral Oligomeric Silsequioxane-Core Star Polystyrene via Nitroxide-Mediated Polymerization. In *Progress in Controlled Radical Polymerization: Materials and Applications. ACS Symposium Series*; Matyjaszewski, K.; Sumerlin, B. S; Tsarevsky, N. V., Ed.; American Chemical Society, 2012; Vol. 1101, pp 141–162. https://doi.org/10.1021/bk-2012-1101.ch010.

(42) Ho, H. T.; Rollet, M.; Phan, T. N. T.; Gigmes, D. "Michael Addition" Reaction onto Vinyl Sulfonyl(Trifluoromethylsulfonyl)Imide: An Easy Access to Sulfonyl(Trifluoromethylsulfonyl)Imide-Based Monomers and Polymers. *Eur. Polym. J.* **2018**, *107*, 74–81. https://doi.org/10.1016/j.eurpolymj.2018.07.042.

(43) Stejskal, E. O.; Tanner, J. E. Spin Diffusion Measurements: Spin Echoes in the Presence of a Time-Dependent Field Gradient. *J. Chem. Phys.* **1965**, *42* (1), 288–292. https://doi.org/10.1063/1.1695690.

(44) Kolín, O.; Dohnal, V. Phase Equilibria in Binary Mixtures of Water with Triglyme and Tetraglyme: Experimental Determination and Thermodynamic Modeling. *J. Chem. Eng. Data* **2020**, *65* (10), 4980–4990. https://doi.org/10.1021/acs.jced.0c00600.

(45) Devaux, D.; Bouchet, R.; Glé, D.; Denoyel, R. Mechanism of Ion Transport in PEO/LiTFSI Complexes: Effect of Temperature, Molecular Weight and End Groups. *Solid State Ionics* **2012**, *227*, 119–127. https://doi.org/10.1016/j.ssi.2012.09.020.

(46) Watanabe, M.; Nagano, S.; Sanui, K.; Ogata, N. Estimation of Li+ Transport Number in Polymer Electrolytes by the Combination of Complex Impedance and Potentiostatic Polarization Measurements. *Solid State Ionics* **1988**, *28–30* (PART 2), 911–917. https://doi.org/10.1016/0167-2738(88)90303-7.

(47) Van Butsele, K.; Stoffelbach, F.; Jérôme, R.; Jérôme, C. Synthesis of Novel Amphiphilic and PH-Sensitive ABC Miktoarm Star Terpolymers. *Macromolecules* **2006**, *39* (17), 5652–5656. https://doi.org/10.1021/ma0606859.

(48) Godovski, Y. K.; Slonimskii, G. L.; Garbar, N. M. Effect of Molecular Weight on the

Crystallization, Melting, Glass-Transition and Morphology in the Ethylene Glycol-Polyethylene Glycol Series. *Polym. Sci. U.S.S.R.* **1973**, *15* (4), 914–931. https://doi.org/10.1016/0032-3950(73)90307-9.

(49) Liang, S.; Choi, U. H.; Liu, W.; Runt, J.; Colby, R. H. Synthesis and Lithium Ion Conduction of Polysiloxane Single-Ion Conductors Containing Novel Weak-Binding Borates. *Chem. Mater.* **2012**, *24* (12), 2316–2323. https://doi.org/10.1021/cm3005387.

(50) Stolwijk, N. A.; Heddier, C.; Reschke, M.; Wiencierz, M.; Bokeloh, J.; Wilde, G. Salt-Concentration Dependence of the Glass Transition Temperature in PEO-NaI and PEO-LiTFSI Polymer Electrolytes. *Macromolecules* **2013**, *46* (21), 8580–8588. https://doi.org/10.1021/ma401686r.

(51) Sun, Y.; Zhang, Z.; Moon, K.-S.; Wong, C. P. Glass Transition and Relaxation Behavior of Epoxy Nanocomposites. *J. Polym. Sci. Part B Polym. Phys.* **2004**, *42* (21), 3849–3858. https://doi.org/10.1002/polb.20251.

(52) Pappenfus, T. M.; Henderson, W. A.; Owens, B. B.; Mann, K. R.; Smyrl, W. H. Complexes of Lithium Imide Salts with Tetraglyme and Their Polyelectrolyte Composite Materials. *J. Electrochem. Soc.* **2004**, *151* (2), A209. https://doi.org/10.1149/1.1635384.

(53) Souquet, J.-L.; Duclot, M.; Levy, M. Salt-Polymer Complexes: Strong or Weak Electrolytes? *Solid State Ionics* **1996**, *85*, 149–157.

(54) Vogel, H. Das Temperaturabhangigkeitsgesetz Der Viskositat von Der Temperatur Bei Unterkuhlten Flussigkeiten. *Phys Z* **1926**, *22*, 645–646.

(55) Tammann, G.; Hesse, W. Die Abhängigkeit Der Viscosität von Der Temperatur Bie

Unterkühlten Flüssigkeiten. *Zeitschrift für Anorg. und Allg. Chemie* **1926**, *156* (1), 245–257. https://doi.org/10.1002/zaac.19261560121.

(56) Fulcher, G. S. Analysis of Recent Measurements of the Viscosity of Glasses. *J. Am. Ceram. Soc.* **1925**, *8* (6), 339–355. https://doi.org/10.1111/j.1151-2916.1925.tb16731.x.

(57) Abraham, K. M.; Jiang, Z.; Carroll, B. Highly Conductive PEO-like Polymer Electrolytes. *Chem. Mater.* **1997**, *9* (9), 1978–1988. https://doi.org/10.1021/cm970075a.

(58) Miyamoto, T.; Shibayama, K. Free-Volume Model for Ionic Conductivity in Polymers. *J. Appl. Phys.* **1973**, *44* (12), 5372–5376. https://doi.org/10.1063/1.1662158.

(59) Murch, G. E. The Haven Ratio in Fast Ionic Conductors. *Solid State Ionics* **1982**, *7* (3), 177–198. https://doi.org/10.1016/0167-2738(82)90050-9.

(60) Gouverneur, M.; Kopp, J.; Van Wüllen, L.; Schönhoff, M. Direct Determination of Ionic Transference Numbers in Ionic Liquids by Electrophoretic NMR. *Phys. Chem. Chem. Phys.* **2015**, *17* (45), 30680–30686. https://doi.org/10.1039/c5cp05753a.

(61) Kataoka, H.; Saito, Y. New Approached for Determining the Degree of Dissociation of a Salt by Measurements of Dynamic Properties of Lithium Ion Electrolytes. *J. Phys. Chem. B* **2002**, *106* (50), 13064–13068. https://doi.org/10.1021/jp020703y.

(62) Feng, Z.; Higa, K.; Han, K. S.; Srinivasan, V. Evaluating Transport Properties and Ionic Dissociation of LiPF 6 in Concentrated Electrolyte . *J. Electrochem. Soc.* **2017**, *164* (12), A2434–A2440. https://doi.org/10.1149/2.0941712jes.

(63) Hayamizu, K.; Akiba, E.; Bando, T.; Aihara, Y. 1H, 7Li, and 19F Nuclear Magnetic Resonance and Ionic Conductivity Studies for Liquid Electrolytes Composed of Glymes

and Polyetheneglycol Dimethyl Ethers of CH3O(CH2CH2O)NCH3 (n = 3 - 50) Doped with LiN(SO2CF3)2. *J. Chem. Phys.* **2002**, *117* (12), 5929–5939. https://doi.org/10.1063/1.1501279.

(64) Dong, D.; Sälzer, F.; Roling, B.; Bedrov, D. How Efficient Is Li+ Ion Transport in Solvate Ionic Liquids under Anion-Blocking Conditions in a Battery? *Phys. Chem. Chem. Phys.* **2018**, *20* (46), 29174–29183. https://doi.org/10.1039/c8cp06214e.

(65) Barrande, M.; Bouchet, R.; Denoyel, R. Tortuosity of Porous Particles. *Anal. Chem.* **2007**, *79* (23), 9115–9121. https://doi.org/10.1021/ac071377r.

(66) Weissberg, H. L. Effective Diffusion Coefficient in Porous Media. *J. Appl. Phys.* **1963**, *34* (9), 2636–2639. https://doi.org/10.1063/1.1729783.

(67) Comiti, J.; Renaud, M. A New Model for Determining Mean Structure Parameters of Fixed Beds from Pressure Drop Measurements: Application to Beds Packed with Parallelepipedal Particles. *Chem. Eng. Sci.* **1989**, *44* (7), 1539–1545. https://doi.org/10.1016/0009-2509(89)80031-4.

TOC Graphic